ARMY RESEARCH LABORATORY

Laser-Based Detection Methods for Explosives

by Chase A. Munson, Jennifer L. Gottfried, Frank C. De Lucia, Jr.,
Kevin L. McNesby, and Andrzej W. Miziolek

ARL-TR-4279   **September 2007**

NOTICES

Disclaimers

The findings in this report are not to be construed as an official Department of the Army position unless so designated by other authorized documents.

Citation of manufacturer's or trade names does not constitute an official endorsement or approval of the use thereof.

Destroy this report when it is no longer needed. Do not return it to the originator.

Army Research Laboratory

Aberdeen Proving Ground, MD 21005-5066

Laser-Based Detection Methods for Explosives

**Chase A. Munson, Jennifer L. Gottfried, Frank C. De Lucia, Jr.,
Kevin L. McNesby, and Andrzej W. Miziolek**
Weapons and Materials Research Directorate, ARL

REPORT DOCUMENTATION PAGE			*Form Approved* *OMB No. 0704-0188*
Public reporting burden for this collection of information is estimated to average 1 hour per response, including the time for reviewing instructions, searching existing data sources, gathering and maintaining the data needed, and completing and reviewing the collection information. Send comments regarding this burden estimate or any other aspect of this collection of information, including suggestions for reducing the burden, to Department of Defense, Washington Headquarters Services, Directorate for Information Operations and Reports (0704-0188), 1215 Jefferson Davis Highway, Suite 1204, Arlington, VA 22202-4302. Respondents should be aware that notwithstanding any other provision of law, no person shall be subject to any penalty for failing to comply with a collection of information if it does not display a currently valid OMB control number. **PLEASE DO NOT RETURN YOUR FORM TO THE ABOVE ADDRESS.**

1. REPORT DATE *(DD-MM-YYYY)*	**2. REPORT TYPE**		**3. DATES COVERED (From - To)**
September 2007	Final		1 May 2005–1 May 2007

4. TITLE AND SUBTITLE	**5a. CONTRACT NUMBER**
Laser-Based Detection Methods for Explosives	
	5b. GRANT NUMBER
	5c. PROGRAM ELEMENT NUMBER

6. AUTHOR(S)	**5d. PROJECT NUMBER**
Chase A. Munson, Jennifer L. Gottfried, Frank C. De Lucia, Jr.,	622618H8049
Kevin L. McNesby, and Andrzej W. Miziolek	**5e. TASK NUMBER**
	5f. WORK UNIT NUMBER

7. PERFORMING ORGANIZATION NAME(S) AND ADDRESS(ES)	**8. PERFORMING ORGANIZATION REPORT NUMBER**
U.S. Army Research Laboratory ATTN: AMSRD-ARL-WM-BD Aberdeen Proving Ground, MD 21005-5066	ARL-TR-4279

9. SPONSORING/MONITORING AGENCY NAME(S) AND ADDRESS(ES)	**10. SPONSOR/MONITOR'S ACRONYM(S)**
	11. SPONSOR/MONITOR'S REPORT NUMBER(S)

12. DISTRIBUTION/AVAILABILITY STATEMENT

Approved for public release; distribution is unlimited.

13. SUPPLEMENTARY NOTES

14. ABSTRACT

Many well-known explosive detection techniques such as mass spectrometry and chromatography rely on close-contact sampling of surface residues or explosive vapors. Effective detection of explosive materials using laser-based methods has been demonstrated in close-contact and standoff (tens of meters) configurations. This work reviews the current technical progress in laser-based explosive detection methods such as infrared spectroscopy, Raman spectroscopy, terahertz spectroscopy, laser-induced breakdown spectroscopy, and photofragmentation. The potential for standoff detection using these techniques is also discussed.

15. SUBJECT TERMS

LIBS, Raman spectroscopy, THz spectroscopy, explosives detection, laser

16. SECURITY CLASSIFICATION OF:			**17. LIMITATION OF ABSTRACT**	**18. NUMBER OF PAGES**	**19a. NAME OF RESPONSIBLE PERSON** Chase A. Munson
a. REPORT UNCLASSIFIED	**b. ABSTRACT** UNCLASSIFIED	**c. THIS PAGE** UNCLASSIFIED	SAR	76	**19b. TELEPHONE NUMBER** (*Include area code*) 410-306-0884

Standard Form 298 (Rev. 8/98)
Prescribed by ANSI Std. Z39.18

Contents

List of Figures

List of Tables

INTENTIONALLY LEFT BLANK.

1. Introduction

Lasers offer multiple approaches for explosives detection that are not possible with other techniques. In general, these can be separated into two types: (1) those based on the unique properties of lasers for long-distance propagation of intense energy and (2) those that are based on the actual molecular and atomic spectroscopy and utilize the high wavelength specificity that most lasers offer. Of course, laser explosives detection is somewhat young given the fact that lasers were invented fairly recently in 1958. As such, it is fair to say that laser explosives detection is still a work in progress, with much having been discovered in recent years, and still more to be discovered in the near future, particularly as more exotic laser sources (e.g., femtosecond lasers) become more common, less expensive, more rugged, and generally, more readily available.

These are very exciting times for the use of lasers for explosives detection. In particular, great progress has been made in solid state lasers and in the extension of laser radiation throughout the infrared, near-infrared, visible, and near-ultraviolet regions with regards to decrease in size and cost for various systems. For example, the neodinium ytterium aluminum garnet (Nd:YAG) laser has become very mature, with improvements over many generations. As a result, one can get reliable laser radiation in the near-infrared fundamental wavelength of 1.06 μm, as well as visible and ultraviolet radiation at the second to fifth harmonics, in a fairly compact and not-too-expensive package.

One particular area where the laser appears to be uniquely capable is in the standoff detection of explosives, where the laser properties of long-distance radiation propagation are providing capabilities not possible with other techniques. Still, although very promising, standoff explosives detection using lasers is an emerging application area requiring time to mature. One other area where lasers offer intriguing potential is in the fusion of orthogonal laser-based techniques, such as laser-induced breakdown spectroscopy (LIBS) and Raman. A number of researchers have started to pursue this avenue because an integrated LIBS/Raman system can use the same laser and spectrometer components. The expected dramatic improvements in probability of detection and reduction of false alarm rates suggest that laser-based explosives detection methods may evolve into a major new technology area in the next 1–3 years.

2. Detection of Explosives Using Laser-Based Vibrational Spectroscopy

Applications of laser-based vibrational spectroscopy to explosives detection have been widely studied. The literature on this topic was summarized by Steinfeld and Wormhoudt (*1*) and by Henderson et al. (*2*). Instrumentation for explosives detection to 2004 was summarized by Moore (*3*).

Detection of explosives depends upon several factors, including physical state of the sample to be detected (solid, liquid, and gas), the vapor pressure of the solid/liquid (if vapor is being detected), a knowledge of spectral characteristics, required sample size and concentration, effects of concealment, spectral interferences, thermal stability, vapor adsorption characteristics, and sampling methods. Figure 1 shows the calculated vapor pressures of the explosives 2,4, dinitrotoluene (DNT), 2,4,6 trinitrotoluene (TNT), and cyclotrimethylenetrinitramine (RDX) over the temperature range of 280–340 K (*4*, *5*). There has been some discussion in the literature as to whether detection of concealed explosives is best accomplished by vapor detection or by detection of particles/explosive-laden fingerprints left behind during placement. For example, a single 5-µm diameter particle of the solid explosive RDX contains as many molecules as a liter of air saturated with RDX vapor at standard temperature and pressure. Additionally, concealment in plastic containers and some formulation ingredients designed to make explosive materials "plastic" may reduce partial pressures of explosive vapors by up to 3 orders of magnitude compared to laboratory values (*1*).
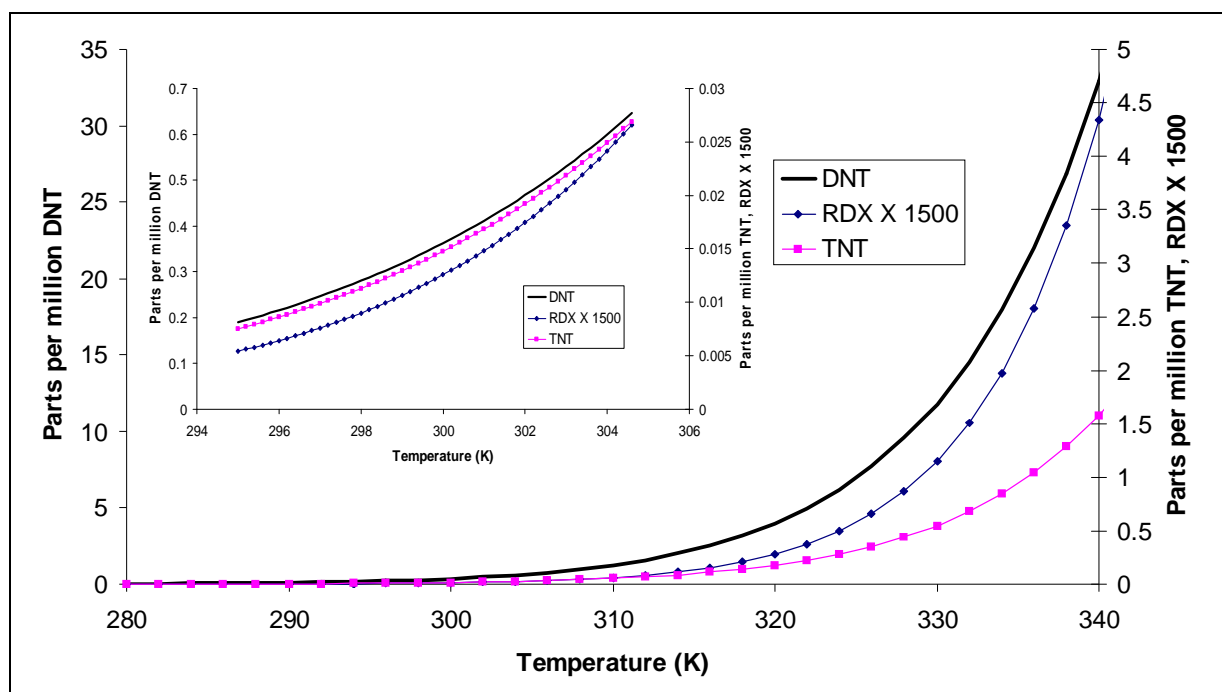
Figure 1. The vapor pressures of the neat explosives 2,4 DNT; 2,4,6 TNT; and RDX over the temperature range of 280–340 K.

Solid or vapor phase vibrational spectra of (unreacted) explosives are usually measured with the bulk sample in the solid state, mainly because most explosives are solids at room temperature (nitroglycerin being the most well-known exception). For many measurements of vibrational spectra of vapors from solid explosives, the solid sample is heated to increase the vapor pressure (*3*). For formulations of high explosives, in which the main ingredient(s) are often crystalline when pure (e.g., C-4, whose main ingredient is RDX), samples may be powders or semimalleable

(plasticized) solids. For low-explosive formulations and propellants, often containing ingredients which are polymeric when pure (e.g., nitrocellulose), samples are often in the form of grains (compressed or formed in the shape of a right circular cylinder), coarse or fine powders, slurries, or solid solutions.

Development of laser-based explosives detection methods employing vibrational spectroscopy begins with characterization of the spectral signature of the explosive to be detected. Spectral signatures of interest are usually those of the neat condensed-phase explosive (e.g., residue left over from a fingerprint) or the vapor emanating from the explosive material (e.g., concealed explosives). Because the vapor pressures of many pure explosive materials are exceptionally low (see figure 1), the vapor above a solid explosive formulation may consist mainly of the most volatile components. Figure 2 shows the infrared absorption spectrum of vapor above solid mil-spec TNT at 340 K (measured by the authors). The measured spectrum is actually vapor-phase DNT, which is an impurity present at several percent in most samples of TNT but with a much higher vapor pressure than TNT (see figure 1) (*6*).
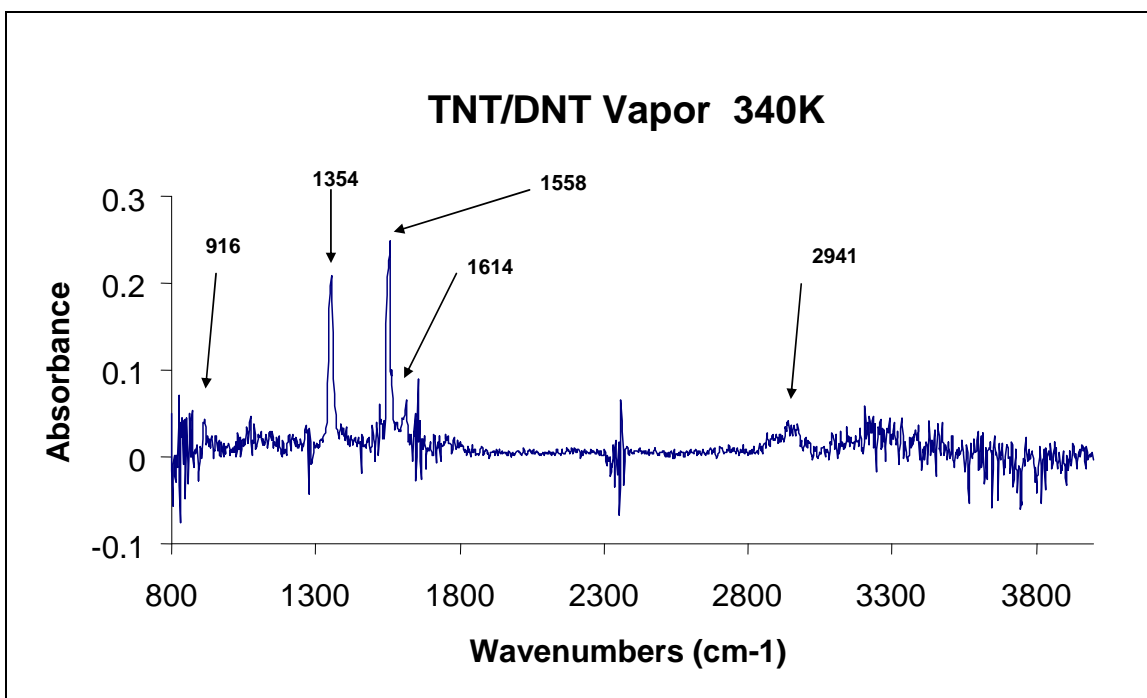
Figure 2. The infrared absorption spectrum of vapor above solid mil-spec TNT at 340 K. The spectrum is identical to that measured above solid DNT at the same temperature (measured by the authors).

Vibrational spectroscopic studies of explosives may be grouped roughly into studies of unreacted materials and products of reaction. Most pre-event detection methods probe unreacted material, although for some explosives, detection methods decomposition products may provide for increased sensitivity (see discussion that follows and section 5.3). Fundamental molecular

vibrations ($\Delta v = 1$) exhibit characteristic frequencies in the mid-infrared spectral region, lying in the wavelength region from 2 to 30 μm ($\sim$300 cm^{-1} to 5000 cm^{-1}). Table 1 shows the infrared spectral regions where many solid explosives and their vapors exhibit features. In general, the most recognizable features of the vibrational spectrum of an explosive are associated with the symmetric and antisymmetric vibrations of the almost ubiquitous –NO$_2$ group, between about 1260 and 1375 cm^{-1} and 1450 and 1600 cm^{-1} (7).

Table 1. Wavenumber ranges and vibrational mode assignments for spectral features commonly observed (650–3100 cm^{-1}) in the infrared absorption spectra of explosives. NO$_2$ symmetric stretches at 1260–1320 and 1325–1375 (indicated in bold) are the strongest infrared (IR) absorption features of explosive materials in the mid-infrared region of the spectrum.

Vibrational Mode Assignment	Explosive (Type)	Wavenumbers (cm^{-1})
NO$_2$ deformation and ring stretch	Nitramine (RDX), TNT	650–850
Ring torsion	Nitramine (RDX),TNT	1000–1080
N-N stretch	Nitramine (RDX)	1200–1230
NO$_2$ symmetric stretch	Nitramine (RDX)	1260–1320
CH$_2$ bend	Nitramine (RDX), TNT	1300–1450
NO$_2$ antisymmetric stretch	Nitramine (RDX),TNT	1450–1600
C-H stretch	Nitramine (RDX), TNT, nitrocellulose	2900–3100
N-O stretch	PETN	850–950
C-C stretch	TNT	1620–1700
NO$_2$ symmetric stretch	TNT	1325–1375
NO$_2$ bend	Nitrocellulose	800–900
NO$_2$ symmetric stretch	Nitrocellulose	1200–1300
NO$_2$ antisymmetric stretch	Nitrocellulose	1600–1700
C-O stretch	PETN	1000–1040

Note: PETN = pentaerythritol tetranitrate.

A significant challenge in using vibrational spectroscopy for explosive detection (especially in the vapor phase) arises because of the combination of low-vapor pressures and relatively low cross section for absorption in the infrared and the low scattering cross section for Raman spectroscopy. For example, typical peak absorption cross sections, α, for the NO$_2$ stretching modes are near 1×10^6 cm^2/mole in the infrared (for comparison, peak ultraviolet [UV] absorption cross sections for TNT approach 50×10^6 cm^2/mole). For Raman spectroscopy, scattering cross sections in the UV may approach 1×10^{-2} cm^2/mole (3, 8).

2.1 Laser Infrared Absorption Spectroscopy of Explosives

Most solid explosives are composed of fairly large molecules with large inertial moments, causing their rotational energy levels to be closely spaced (9). The infrared absorption spectra of many neat solid explosives appear as fairly broad features resulting from the blending together of rovibrational lines corresponding to a given vibrational transition. The broad spectral features of many solid explosives (including their vapors) in the infrared lend themselves to measurement by broad band techniques such as Fourier-transform (FT) infrared spectroscopy (10). Laser-based

methods of detection by infrared absorption techniques are often limited by the bandwidth of the light source (this is not necessarily the case with Raman spectra of many neat solid explosives; for this reason, Raman spectroscopy has been used extensively for analysis of solid explosives (*11*) (see section 2.2).

2.1.1 Tunable Diode Laser Spectroscopy (TDLAS)

TDLAS uses mid- and near-infrared semiconductor light sources and detectors (similar to those used in CD players and laser pointers) to measure (usually minute) changes in light intensity caused when the light beam passing through a region of space containing an explosive/explosive gas is partially absorbed. TDLAS can achieve high sensitivity by virtue of phase sensitive detection, combined with modulation techniques that discriminate against 1/f noise of the laser source (*12*). Light sources are commercially available throughout the mid- and near-infrared spectral region. Recent developments in the last decade of quantum cascade (QC) and interband cascade lasers offer the promise of room temperature, continuous wave operation throughout the infrared fingerprint region (3–16 µm) (*13*). An illustration of the measurement process using the Beer-Lambert Law is shown in figure 3.

Absorption Spectroscopy–Beer-Lambert Law:

$$I_t = I_0 \exp(-s\,LN)$$

s = absorption coefficient
L = path length
N = number of absorbers

Limitation: Measurement of small difference between two large numbers

source $\rightarrow$ I_0 Vapor from explosive $\rightarrow$ I_t detector
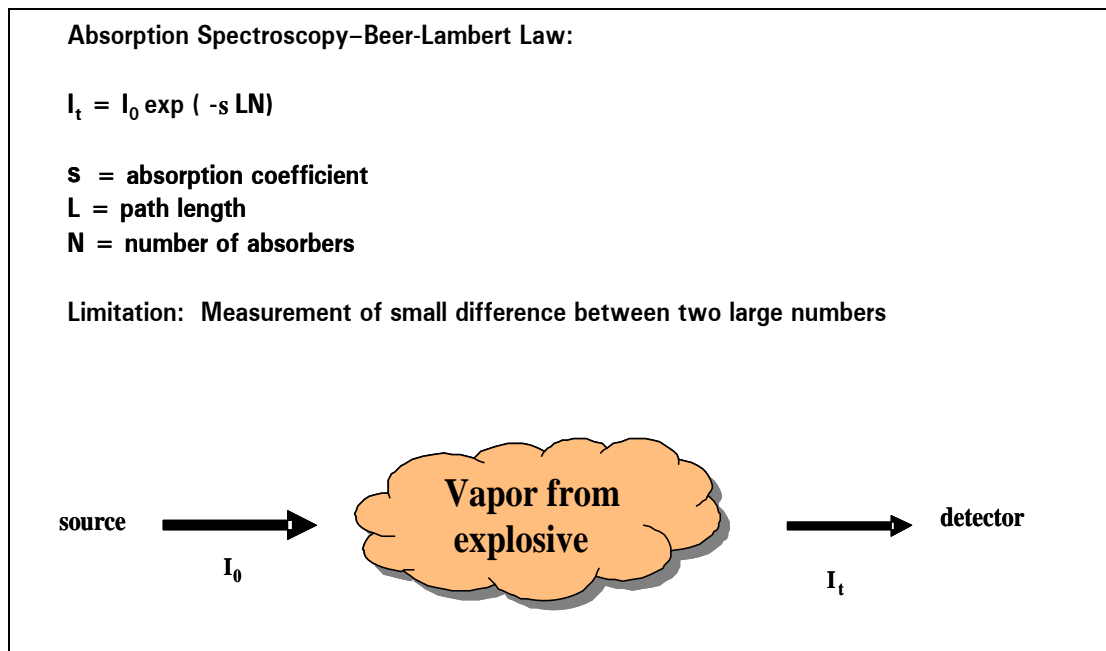
Figure 3. A cartoon schematic of the application of the Beer-Lambert Law to explosive vapor sensing.

Applications to explosives sensing using semiconductor light sources have been reviewed by Allen et al. (*14*). Traditional detection methods (Beer-Lambert law-type experiments) are somewhat limited because the broad spectral features of many neat explosive vapors make phase sensitive detection methods difficult (*10, 12*). Because of this, TDLAS is often used to detect and measure light gases (e.g., NO and NO_2) produced by decomposition of the parent explosive.

Wormhoudt et al. (*15*) used a near-infrared diode laser to measure NO produced during hot filament pyrolysis of TNT in soils. Riris et al. (*16*) used a lead-salt TDL to detect NO_2 produced following catalyzed thermal decomposition of 5–10 pg of RDX in a heated sample cell. TDLAS is often used in tandem techniques to detect explosive fragments produced by photofragmentation of the parent explosive. For example, Bauer et al. (*17*) have used a QC mid-infrared laser to detect NO produced by 1.55-μm laser photofragmentation of TNT and RDX.

2.1.2 Optical Parametric Oscillators (OPOs)

OPOs provide an alternative method of generating coherent radiation in the infrared spectral region and may exhibit a broad tuning range. An OPO converts an input laser wave (ω_p – pump frequency) into two output waves of lower frequency (ω_s – signal frequency and ω_i – idler frequency) by means of nonlinear (usually crystal borne) optical interaction. The sum of the output wave frequencies is equal to the input wave frequency: $\omega s + \omega i = \omega p$. Employing a nonlinear optical crystal for frequency conversion, quasi-phase-matching may be accomplished by periodically changing the nonlinear optical properties of the crystal (periodical poling). For example, output wavelengths from 700 to 5000 nm can be produced in periodically poled lithium niobate. Common pump sources are Nd:YAG lasers at 1.064 or 0.532 μm. Effenberger and Mercado (*18*) used an OPO-based system that used idler (mid-IR output) and signal (near-IR output) in a differential absorption experiment and were able to detect explosive vapors to 1 ppm. OPOs have also been used as the light source for cavity-enhanced detection methods (*19*) and for light detection and ranging (LIDAR) and differential absorption LADAR (DIAL) methods (*20*) (also see sections 2.3 and 5.5).

2.1.3 Detection Using CO_2 Lasers

Although carbon dioxide lasers offer limited line-tunability from a 9- to 11-μm wavelength, the significant output power makes them amenable to some methods of explosives detection. CO_2 lasers also see application as light sources in some photoacoustic measurement schemes (see section 5.4). For example, Chaudhary et al. (*21*) have used a CO_2-based photoacoustic technique to detect ppb (by weight) amounts of TNT and RDX. McKnight et al. (*22*) have used the acoustic pulse from a focused CO_2 laser employing different spot sizes to identify buried objects. The authors of this work concluded that the unfocused 1.1×0.7 cm produced better underground acoustic imaging of buried objects.

2.1.4 Difference Frequency Generation Spectroscopy

Kim et al. (*23*) have used vibrational sum-frequency generation spectroscopy (SFG) to characterize the surfaces of β-octahydro-1,3,5,7-tetrocine (HMX) single crystals, as well as the interface between HMX and the copolymer Estane.[1] SFG is a nonlinear vibrational spectroscopic technique related to optical parametric amplification that selectively probes vibrational transitions

---

[1]Estane is a registered trademark of BF Goodrich.

at surfaces and interfaces. Compared to bulk HMX, the surface vibrational features are blueshifted, and observed splittings are larger. The technique may have application to detection of explosive residues on surfaces.

2.1.5 Cavity Ringdown Spectroscopy (CRDS)

CRDS is a technique used to enhance measured absorption of light by a chemical species by greatly increasing the light path through the sample (see figures 3 and 4). This is achieved by placing the sample within an optical cavity that uses two highly reflective mirrors to create a stable optical resonator, such that the alignment of the reflective mirrors on each end of the cavity serves to "trap" light within the cavity. When a pulse of light enters the cavity, it can make thousands of round trips before its intensity dies off, resulting in effective path lengths of kilometers. The decrease in intensity with time, called "ringdown time," is measured by allowing a small amount of light to leak through one of the mirrors to impinge on a fast photodetector. Contributions to the ringdown time by species absorption of light may be readily separated from other causes of loss of intensity (scattering, mirror imperfection, etc.). A scan of ringdown time vs. wavelength can yield the absorption spectrum of a species present in extremely low concentrations. This is shown schematically in figure 4.

Ringdown Cavity

Detector

Laser

Mirror   Mirror

1. The ring-down rate of an optical cavity depends on losses caused by transmission of the mirrors and scattering and/or absorption by species inside the cavity.

Absorption spectrum is recorded by measuring ringdown rate as a function of wavelength

2. The Ring Down Rate is independent of noise and reproducibility of light source.

Ringdown Signal

Figure 4. A description of a CRDS apparatus.

Busch and Busch (*24*) have reviewed the technique and applications of CRDS to trace sensing to 1999. Two reviews (*25, 26*) discuss CRDS applications to explosives. Dagdigian (*27*) has written a review of optical methods, including CRDS, employed for detection of decomposition

of explosives and energetic materials. Todd et al. (*19*) have used a mid-infrared OPO to measure vapor-phase mid-IR spectra of common explosives (TNT, triacetone triperoxide [TATP], RDX, PETN, and Tetryl[*]) using the CRDS technique. Parts-per-billion concentration levels were detected with no sample preconcentration. A collection/flash-heating sequence was implemented to enhance detection limits for ambient air sampling. Detection limits were not determined but were expected to approach 75 ppt for TNT, with similar concentration levels for the other explosives.

2.2   Laser Raman Spectroscopy

Analytical techniques based upon Raman spectroscopy have been widely used for explosive detection and characterization. Following theoretical prediction of inelastic light scattering in transparent media (*28*), the effect was experimentally verified in liquids by Raman in 1928; this phenomenon is known as the "Raman effect." The first demonstration of the Raman effect in gases was demonstrated by R. W. Wood (HCl gas) and F. Rasetti (CO and CO_2). The frequencies observed in Raman scattering correspond to the frequency of the incident light shifted by some characteristic frequency of the scattering molecule. The difference in energy between the incident and scattered photons (the Raman spectrum of the molecule) is typically a function of the vibrational energy levels within a molecule.

Prior to the invention of the laser, Raman spectroscopy relied on arc lamps to provide incident light, and long periods of exposure were necessary to record a spectrum. The advent of high intensity, monochromatic laser radiation generated renewed interest in Raman spectroscopy in the 1960s. The implementation of FT spectrometers and lasers with output wavelengths that minimized sample fluorescence increased the utility of the technique and fostered application to explosive analysis.

Chemical species that exhibit a change in polarizability with vibration (including all known neat molecular explosives) exhibit Raman spectra that are uniquely determined by their vibrational mode structure. Laser Raman spectroscopy has been shown to be a valuable technique for the characterization of many explosives and explosive formulations, especially those containing molecular crystals (e.g., RDX) (*29, 30*). Reasonably good spectra of neat polymeric samples (e.g., nitrocellulose [NC]) may also be obtained. However, Raman spectroscopy may be limited for bulk analysis of many colored formulations of polymeric energetic materials (NC containing formulations are often colored, e.g., JA2,[†] M9,[‡] M30,[§] which range in color from dull yellow to almost black) and for other colored samples (even slightly yellow crystals of impure TNT). These samples tend to absorb the scattering radiation and decompose or heat up to an extent that the Raman signal is overwhelmed by a thermal signature. Because Raman line widths are

---

[*]2,4,6-trinitrophenyl-N-methylnitramine.

[†]JA2 = NC (60%), NG (15%), DEGDN (25%).

[‡]M9 = NC (60%), NG (40%).

[§]M30 = NQ (50%), NC (30%), NG (15%).

narrower than those measured using absorption-based measurements, it is possible to see slight impurities in samples and in mixtures of many explosive materials. Laser Raman spectra of the explosive formulation C-4, its main ingredient RDX, and samples of RDX of different origin are shown in figure 5 (*11*).
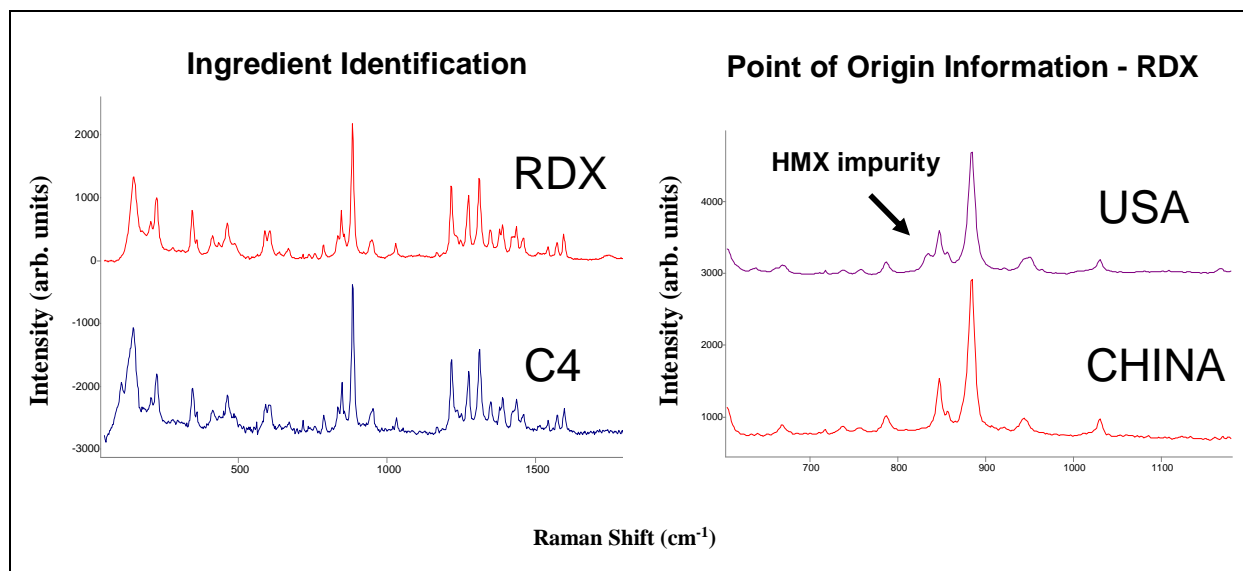
Figure 5. Laser FT-Raman spectra of the explosive formulation C-4, its main ingredient RDX, and samples of RDX of different origin. The exciting laser wavelength was 1064 nm (*11*).

The first review of laser Raman spectroscopy of explosives appeared in the late 1960s (*31*). A patent application for laser Raman applied to the remote identification of hazardous gases from explosives decomposition was filed a few years later (*32*).

Because many explosive samples fluoresce when exposed to visible laser radiation, the use of Raman spectroscopy for explosives analysis was accelerated by the development of near-IR laser sources and FT Raman techniques. Beginning in the late 1970s, FT-Raman spectroscopy began to be used for analysis of propellants and energetics characterization (*33*). Also around this time, coherent anti-Stokes Raman spectroscopy (CARS) began to be developed for explosives analysis (*34*). In CARS, two laser frequencies—a pump frequency (ω_1) and a tunable frequency (ω_2)—are mixed and focused onto the target species, producing a third coherent frequency (ω_3), where $\omega_3 = 2\,\omega_1 - \omega_2$. When $\omega_1 - \omega_2$ is equal to the frequency of a Raman transition in the molecule, the CARS signal intensity increases. As a result, a CARS spectrum can be produced by scanning ω_2 and recording the resulting CARS intensity. The use of laser Raman spectroscopy for the trace identification of energetic materials was first reported by Carver and Sinclair, with limits of detection of 1 ng or less for RDX, PETN, and TNT (*35*). Trott and Renlund (*36*) reported single pulse Raman studies of the solid explosive triaminotrinitro benzene (TATB).

As laser FT-Raman spectroscopy found wider use, Raman spectroscopy, in general, found wider application to the study of energetic materials. Survey FT-Raman spectra of most common explosives and propellants were reported in the early 1990s (*29*, *30*, *37*). CARS for real-time diagnostics of explosions was first reported in 1991 (*38*). Hare et al. used picosecond Raman spectroscopy to study energy transfer in shock-initiated explosives (*39*). Gupta used fast-time resolved Raman spectroscopy to study the flow of vibrational energy behind a shock wave in nitromethane (*40*). Also around this time, the use of the Renishaw Raman microscope for explosive detection and analysis was first reported (*41*). Limits of detection for most explosives studied were in the picogram range.

During this time, there was an increasing effort to employ Raman spectroscopy as a tool in a field deployable explosives detector (*42*). Demonstration of enhancement of the Raman signal as the wavelength of the incident light approaches the wavelength of an allowed transition (resonance Raman spectroscopy) and the elimination of fluorescence when using incident radiation near 244 nm were first reported for explosives in 1997–1998 (*43*, *44*). Raman measurements on dilute TNT and DNT solutions in acetonitrile with 248-nm laser excitation have shown that for the -NO_2 stretching Raman modes, there is significant resonant enhancement (*8*). For TNT, the Raman cross section of the 1351.6 cm^{-1} -NO_2 stretching mode is 5.18 ($\pm$0.4) 10^{-26} cm^2/molecule, and for 2,4-DNT, the Raman cross section of the 1351.3 cm^{-1} -NO_2 stretching mode is 7.25 ($\pm$1.1) 10^{-26} cm^2/molecule. In 2006, Blanco et al. (*45*) have described the use of resonance Raman spectroscopy for measurement of trace amounts of DNT and TNT dispersed in sands and soils. Pattern recognition algorithms and the use of neural networks and principal component analysis for classifying Raman spectra of explosives appeared in the late 1990s (*46–48*).

The use of surface enhanced Raman spectroscopy (SERS) for trace explosive detection was first investigated during the late 1990s (*49*). In SERS, an enhancement in Raman intensity is observed by placing the sample in close contact with a metallic surface, typically gold or silver nanoparticles. This effect is caused by surface plasmon resonance. Soon thereafter (*50*), SERS detection of 2,4-DNT vapor to ~1 ppb was demonstrated. Within a year (*51*), a field portable unit had demonstrated a limit of detection of 5-ppb vapor DNT and the ability to locate buried land mines. More recently, nanoengineered SERS substrates have been employed, and ppb sensitivity for some nerve agent and explosive simulants has been demonstrated (*52*). Baker and Moore (*53*) have published a review of the literature to 2005, focusing on SERS techniques and substrate development for explosives detection.

Dieringer et al. (*54*) have reported advances in single molecule SERS (SMSERS). Excitation of the localized surface plasmon resonance (LSPR) of a nanostructured surface or nanoparticle determines signal strength and reproducibility. Important design criteria of the SMSERS substrate for maximum excitation of LSPR include material, size, shape, interparticle spacing, and dielectric environment. Nanosphere lithography for the fabrication of highly reproducible and robust SERS substrates is described.

2.3 Laser-Based Standoff Detection Methods

Laser-based standoff explosive detection methods employing vibrational spectroscopy are usually of the type described as LIDAR. In general, light detection and ranging involves launching a series of short laser pulses into the air or towards a target. These light pulses are scattered in all directions by the target (particles, aerosols in the atmosphere, hard surface targets, etc.). A gated, sensitive light detector measures the time and wavelength of the scattered light that returns to the source. The transit time determines the range of the scattering object, aerosol, or chemical species. If the scattered light is Raman shifted and analysis of the Raman shift is used to identify chemical species, the technique is usually called Raman LIDAR. If the LIDAR technique employs two mid- or near-infrared pulsed lasers and determines the identity of chemical species by measuring the differential absorption between two pulses with similar transit times, the technique is usually called differential absorption LIDAR, or DIAL.

LIDAR analysis grew out of National Aeronautics and Space Administration programs on remote winds and aerosols measurements of the late 1960s. The potential for performing remote Raman analysis of species with visible laser excitation in the atmosphere was explored as early as 1973 (*55*, *56*). Bulk and surface materials were explored in the 1990s (*57*, *58*). Sharma et al. (*59*) have measured Raman spectra of TATB and HMX at 10 m (see figure 6). Standoff Raman spectroscopy has been demonstrated for detection of organic materials at ranges of 100 m using 532 nm (*60*) and 500 m using a UV laser and large collection optics (*61*).
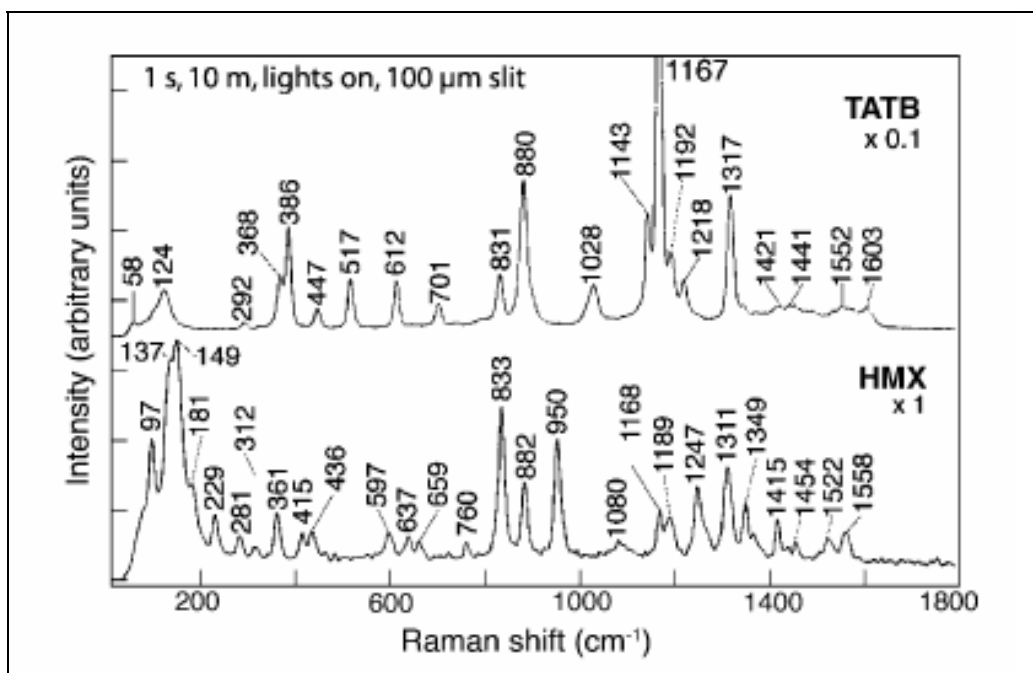
Note: Used with permission from Sharma et al. (*59*).

Figure 6. Remote Raman spectra of explosives TATB and HMX at a standoff distance of 10 m.

11

As mentioned previously, in addition to the $(1/\lambda^4)$ increase of the Raman scattering cross section with UV excitation, further enhancement can also occur when the excitation frequency approaches an electronically excited state of the molecule (*8*, *62*). This resonance Raman enhancement can range from factors of 2–3× to orders of magnitude. Fluorescence is suppressed because the onset typically occurs at excitation wavelengths above ~270 nm (*63*, *64*). Resonance Raman detection is in the solar-blind region, so resonance Raman UV LIDAR can be operated both during day and night time. In the case of Raman LIDAR, the signal will be attenuated because of large absorption due to ozone and higher molecular scattering at 248 nm (*65*).

Carter et al. (*66*) have used a standoff Raman system for detecting explosive materials at distances to 50 m in ambient light conditions. In the system, light is collected using an 8-in Schmidt-Cassegrain telescope fiber-coupled to an f/1.8 spectrograph, with a gated intensified charge-coupled device detector. A frequency-doubled Nd:YAG (532 nm) pulsed (10-Hz) laser is used as the excitation source for measuring remote spectra of samples containing 8% explosive materials. The explosives RDX, TNT, and PETN, as well as nitrate- and chlorate-containing materials, were used to evaluate the performance of the system. Laser power and detector gate width studies were performed to determine the effects of laser heating and photodegradation (significant for TNT residues) and evaluate performance in high levels of ambient light (e.g., sunlight).

Schultz et al. (*13*) have investigated monostatic and bistatic frequency modulated, differential absorption LIDAR (DIAL) at standoff distances to 2.5 km. This group is also evaluating miniature QC laser transmitters for multiplexed chemical sensing. Vaicikauskas et al. (*20*) have used infrared differential absorption LIDAR (IRDIAL) capable of sensing pollutant gases at distances up to several kilometers.

Ultraviolet mini-Raman LIDAR for standoff, in situ identification of chemical surface contaminants has been reported (*67*). Using semiportable equipment, UV Raman spectroscopic identification of bulk organic compounds at distances of over half a kilometer has been demonstrated (*61*). Also, UV Raman measurements employing a 248-nm KrF excimer laser have been developed for detecting surface contamination with chemical agents and explosives to intermediate standoff distances (*68*).

2.4   Future Directions

Laser-based detection of explosives using vibrational spectroscopy is not yet a mature science. For solid residue detection, methods exist that can detect the explosive, as long as the area to be investigated has been preselected. For vapor phase detection, the inherently small infrared absorption and Raman cross sections, combined with low vapor pressures of most solid explosives, make detection extremely difficult. Some areas for improvement are in power and tuning range of ultra narrow-band light sources (especially in the mid-IR), scan rates of high-power pulsed laser sources, incorporation of ultra-fast (fs, as) laser sources that employ filamentation for long-range power delivery, compact high-power sources to help move

equipment out of the lab, quantum-control of laser pulses for enhancement of absorption cross sections, new modulation techniques, low power consumption fast detectors, and improved spectrographs.

3. LIBS

A relatively new method for optically detecting explosives is LIBS. LIBS is an atomic emission spectroscopy technique used for the real time, nondestructive determination of elemental composition and requires no sample preparation. The technique relies on a microplasma created by a focused laser pulse, typically several nanoseconds in length, to dissociate molecules and particulates within the plasma volume. The subsequent emission can be resolved spectrally and temporally in order to generate a spectrum containing emission lines from the atomic, ionic, and molecular fragments created by the plasma. A single laser shot and subsequent data analysis can take place in under a second. The basic LIBS experimental setup is shown in figure 7. Typically, a Nd:YAG laser is used to produce a pulse width of a few nanoseconds. This laser pulse is focused onto the sample surface. When the laser power at the focal point exceeds ≈ 1 GW/cm^2, a microplasma is created. Emission from the microplasma is then collected by a series of lenses and delivered to a spectrometer in order to resolve the collected light. Finally, the spectrally resolved light arrives at a detector in order to generate a LIBS spectrum. An example is shown in figure 8.
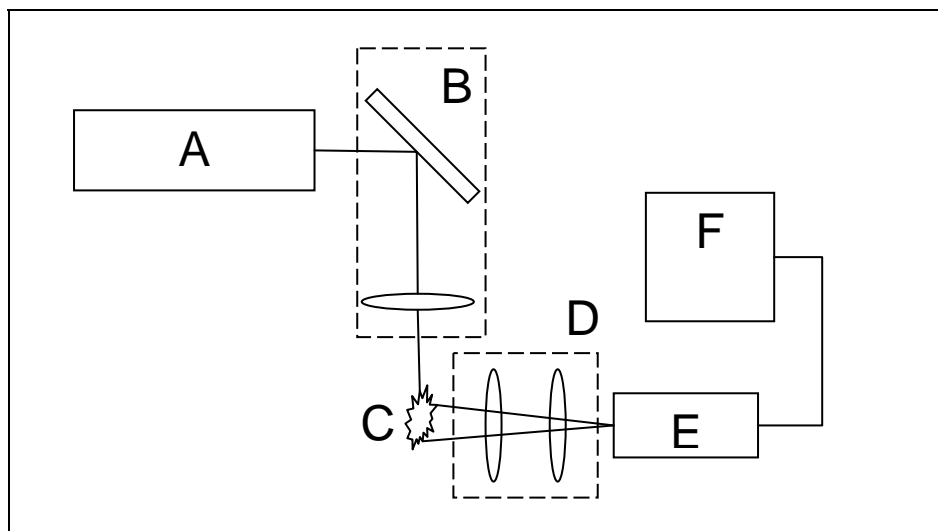
Figure 7. Block diagram of laser induced breakdown spectroscopy experimental setup (A) pulsed laser, (B) focusing optics, (C) microplasma, (D) collection optics, (E) spectrometer, and (F) data analyzer.
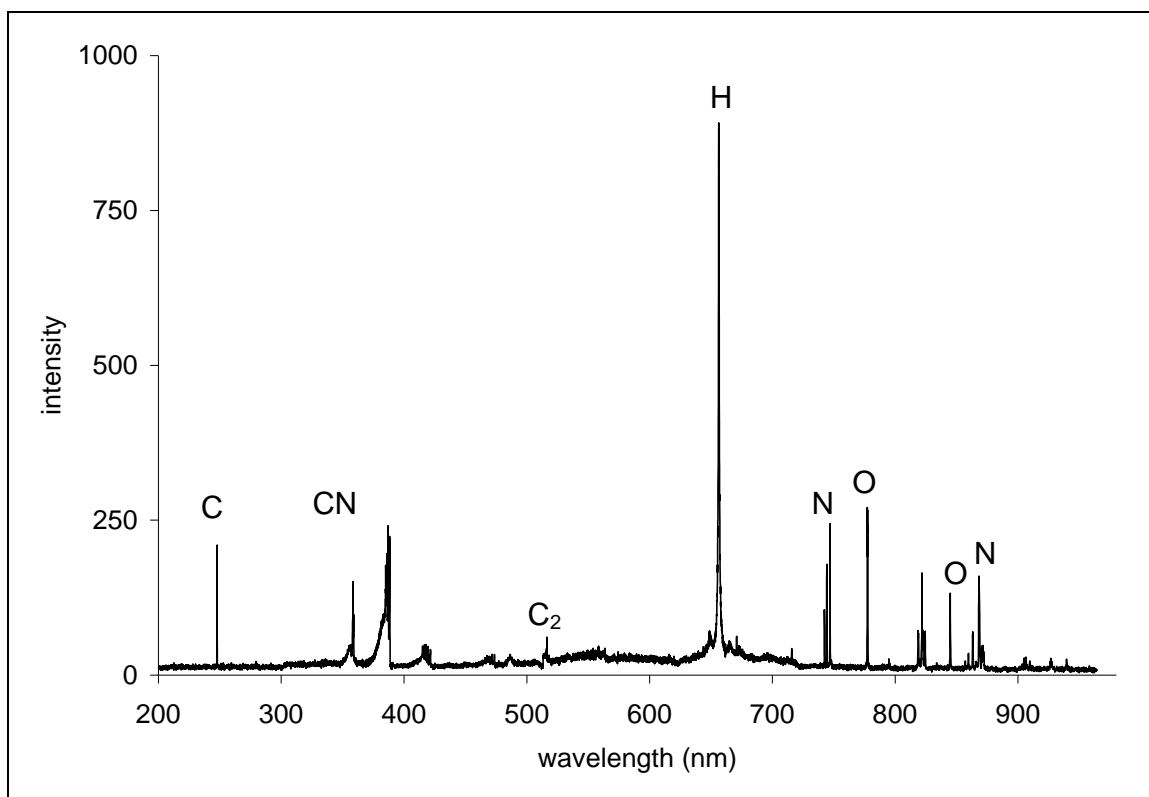
Figure 8. Single-shot LIBS spectrum of type I plastic collected from a 320-mJ, 8-ns laser pulse.

In the past, LIBS has been primarily used to analyze one or a few elements, mostly metals (*69–71*). More recently, with the advent of high resolution, broadband spectrometers, the capability of LIBS to identify compounds could be realized. Every element on the periodic table has atomic emission lines that emit in the visible spectrum. A broadband spectrometer allows one to capture all of the elements in the sample interrogated by the laser-generated plasma, provided they are present in sufficient abundance. Instead of concentrating on a small portion of a LIBS spectrum, all the emitting elements in a sample can be observed in a full broadband LIBS spectrum. Thus, the presence of atomic emission lines and the relative intensity of the atomic emission lines to one another can be used to identify the sample. Now LIBS can more readily be applied to a variety of materials beyond metals, including plastics and other organic compounds, biological materials, and other hazardous compounds (*72–78*). The carbon, hydrogen, oxygen, and nitrogen atomic emission lines are commonly used to identify organic compounds. Figure 8 is an example of a LIBS spectrum of plastic. A prominent carbon atomic emission line is located at 247 nm. A hydrogen atomic emission line, the H_α line, emits at 656 nm. Oxygen atomic emission lines due to neutral oxygen (O I) can be observed at 777 and 845 nm. Nitrogen atomic emission lines due to neutral nitrogen (N I) can be observed at 744, 746, and 868 nm. The atomic emission lines of elements associated with organic compounds demonstrates the necessity of using a broadband spectrometer (200–1000 nm) for identifying these compounds. Anzano et al. (*72*) used LIBS to see if linear correlation techniques would allow sorting of a variety of

plastics, including polystyrene and high density polyethylene. Subtle differences in intensities allowed successful identification 90%–99% of the time. Portnov et al. (*76*) used LIBS to investigate the spectral signatures of nitroaromatic and polycyclic aromatic hydrocarbon samples. They observed the atomic emission lines associated with C, H, N, and O, but they also observed emission due to molecular fragments associated with the CN ($B^2\Sigma$–$X^2\Sigma^+$) violet system and the C_2 (d $^3\Pi$g–a $^3\Pi$u) Swan system. These fragments were used to successfully show differences between the compounds studied. Ferioli and Buckley (*74*) have used LIBS to study hydrocarbon air mixtures (C_3H_8, CH_4, and CO_2 in air). The strength of the C, N, and O atomic emission lines is investigated in relation to the concentration of carbon and hydrogen present in the samples.

In addition to using the absolute intensities of the atomic emission lines, the peak intensity ratios of these lines have been used to analyze samples. Tran et al. (*78*) analyzed the atomic intensity ratios of several organic compounds with the hope to determine the empirical formula of a compound based on the ratios from several elements. Calibration curves were built based on C:H, C:O, and C:N atomic emission ratios from a variety of compounds that covered a wide range of stoichiometries. Then, four compounds with known stoichiometries were tested against the calibration curves. The ratios determined from the calibration curves were compared with the actual stoichiometries and showed accuracy of 3% on average. In the study of nitroaromatic and polycyclic aromatic hydrocarbon samples, the ratios between C_2 and CN and between O and N of different samples were shown to correlate with the molecular formula (*76*). Anzano et al. (*72*) also attributed success of their correlation of plastics to differences in the C/H atomic emission intensity ratio of each sample.

3.1 LIBS of Explosives

LIBS has been shown to be a successful avenue for detecting organic material and, in some cases, determining the type of organic material. Applying LIBS to energetic organic material detection and identification is of interest for a variety of applications, including force protection, security concerns, forensic analysis, etc. The success of LIBS for identifying organic compounds based on atomic emission intensity ratios led researchers at the U.S. Army Research Laboratory (ARL) to investigate characteristics of LIBS spectra of explosive compounds. LIBS spectra were collected from a variety of explosive materials, including highly purified RDX, HMX, TNT, PETN, and NC as well as operational explosive and propellants C-4, A-5, M-43, LX-14, and JA2 (*79*). All of the expected atomic lines—carbon, hydrogen, nitrogen, and oxygen—are present. They also discuss how an energetic organic compound might be discriminated from other materials by using the oxygen to nitrogen atomic emission intensity ratio. The scheme to identify energetic compounds vs. nonenergetic organic compounds is rooted in the observation that energetic materials have larger amounts of oxygen and nitrogen relative to carbon and hydrogen. For example, the chemical formulas of RDX and TNT are $C_3H_6N_6O_6$ and $C_7H_5N_3O_6$, respectively. Some potential interferents include super glue,

$C_{10}H_{10}O_4N_2$, plastics, repeating hydrocarbon chains of some sort, or nylon, $(C_{12}H_{22}O_2N_2)_n$. As can be seen, oxygen and nitrogen are in much greater abundance in the explosives relative to the carbon and hydrogen. In order to identify energetic materials, it is necessary to track the carbon, hydrogen, oxygen, and nitrogen emission lines, as well as the oxygen and nitrogen atomic emission intensities relative to those of carbon and hydrogen.

The following example illustrates how LIBS spectra may be applied to explosives detection. RDX was dissolved into acetone and then applied to an aluminum substrate. A thin residue of RDX was left after the acetone evaporated. LIBS spectra collected from RDX on aluminum and plain aluminum are shown in figure 9. No carbon or hydrogen atomic emission line is present in the plain aluminum sample. In order to eliminate the nitrogen and oxygen contribution from the atmosphere, LIBS spectra were also collected with the sample under argon. The composition of atmosphere is ~80% nitrogen and ~20% oxygen—a 1:4 oxygen to nitrogen ratio. In RDX $(C_3H_6N_6O_6)$, the oxygen to nitrogen stoichiometric ratio is 1:1. In the LIBS spectra in figure 9, the intensity ratio of oxygen atomic emission line intensity to nitrogen atomic emission line intensity from RDX in air is ~2. The intensity ratio of oxygen to nitrogen from RDX in argon is ~5. The increase in the oxygen to nitrogen intensity ratio demonstrates the ability of LIBS to track relative amounts of elements in a sample. In this case, the increase of oxygen relative to nitrogen when air is displaced by argon shows that the oxygen and nitrogen atomic emission line intensities are entirely due to RDX and not from atmospheric oxygen and nitrogen.
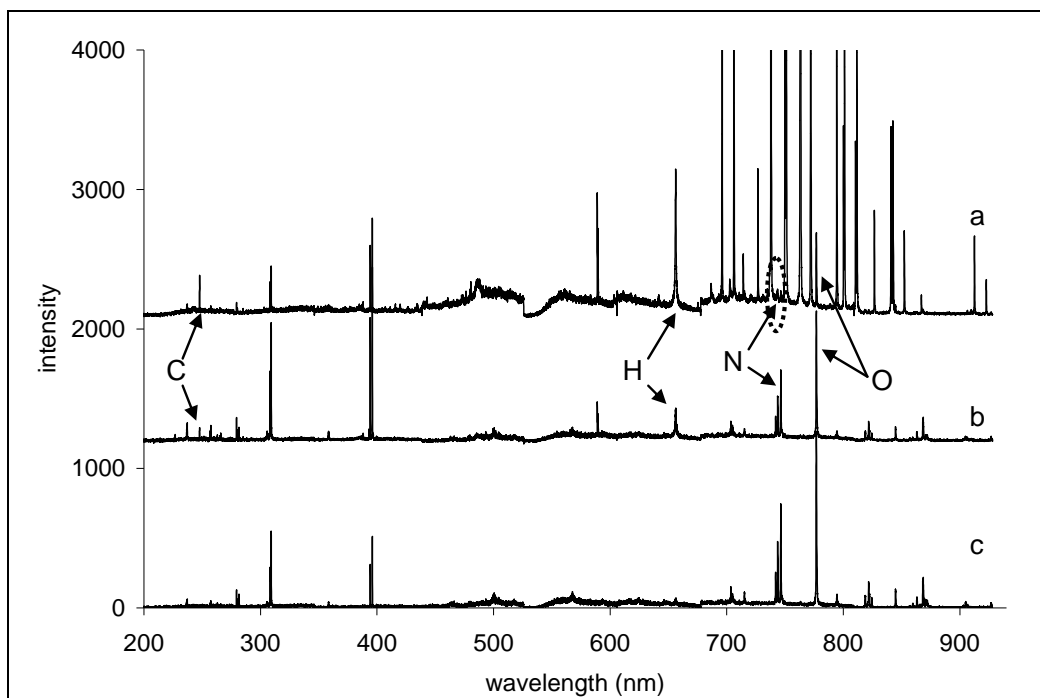
Figure 9. Single-shot LIBS spectra collected with man-portable LIBS system of (a) RDX residue on aluminum under argon, (b) RDX on aluminum in ambient atmosphere, and (c) plain aluminum in ambient atmosphere. Carbon (C), hydrogen (H), nitrogen (N), and oxygen (O) are shown for the RDX samples.

3.2 LIBS Systems

The standard laboratory LIBS system has been described in figure 7. Due to the simplicity of the setup, different types of configurations can be used, depending on the application. In particular, systems can be developed for field use (*73*, *80*). Small rugged lasers and spectrometers can be used for portable instruments. LIBS biggest impact may be in the field. At ARL, a man-portable instrument was recently developed (*73*). A small Nd:YAG laser is contained in a hand-held wand. The focusing optics and collection optics are also in the wand. The collected light is delivered to a backpack spectrometer via a fiber-optic cable. Then, the data is analyzed by an onboard computer and displayed in a heads-up display. A variety of LIBS spectra has been collected using the unit ranging from plastic land mine casings to liquid chemical warfare simulants (*73*). In figure 9, the LIBS spectrum of the RDX residue on aluminum was collected by the man-portable LIBS system. The carbon, hydrogen, oxygen, and nitrogen are all from the RDX residue because the sample is taken under argon.

Another configuration for LIBS in the field is a standoff system capable of sampling tens of meters away from the instrument. In this case, a higher power laser is used in conjunction with telescopic optics that focuses the laser and collects the light from the plasma. Several optical configurations to achieve telescopic focusing and collecting for standoff operation have been used (*81–84*). Standoff LIBS has been used for a variety of applications, most typically elemental analysis. Recently, a standoff system was used to collect LIBS spectra of explosive residues at 30 m (*82*). A blind test was performed that included explosive residues of TNT and C4 as well as nonenergetic organic materials such as a human fingerprint and car paint. Post-data analysis correctly predicted an explosive material or a nonexplosive material six out of six times. More recently, a standoff system was developed for ARL. A LIBS spectrum of RDX on a painted substrate collected at 20 m using the standoff system is shown in figure 10.

3.3 LIBS Future

One of the biggest obstacles to explosives detection is interference from oxygen and nitrogen in the atmosphere. The atmospheric nitrogen and oxygen must be diminished in order to get a more accurate intensity ratio and identify energetic materials from background materials. There are several methods that can be employed to minimize oxygen and nitrogen from the atmosphere. As described earlier (section 3.1), argon could be used to blow across the surface and displace atmospheric oxygen and nitrogen. While this method is effective for close contact studies, it cannot be used with standoff applications. Two methods that may have promise for explosive detection at a standoff distance are double-pulse LIBS and femtosecond LIBS. Double-pulse LIBS involves two pulses aligned collinearly, separated by a few microseconds, interacting with the sample. Advantages of double-pulse LIBS include an increased signal and better reproducibility from shot to shot (*85–88*). The reason for the increased signal has been attributed to several factors including greater mass ablation, a wider region of high temperature in the
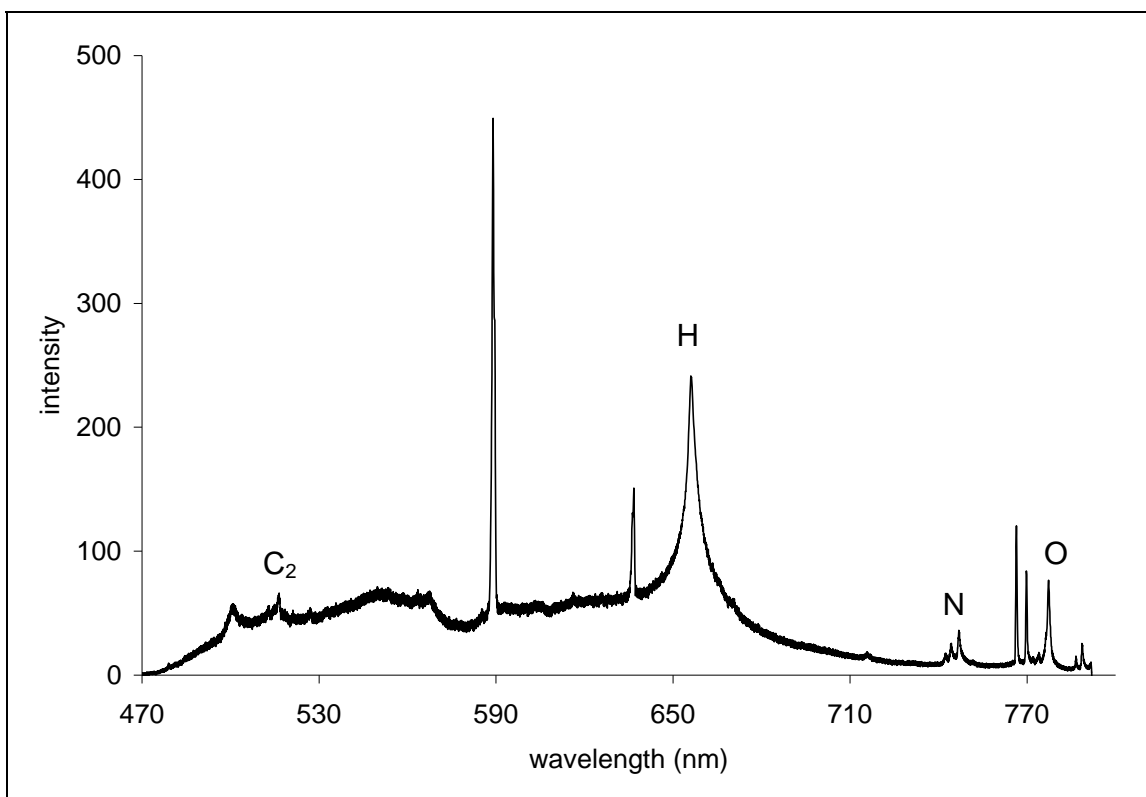
Figure 10. LIBS spectrum of RDX collected at 20 m with the ARL standoff LIBS system. The elements present due to RDX are labeled.

plasma so more atoms are excited, and less laser shielding due to a decrease of gas density (*85*). It is the last of these factors, the decrease in gas density, which allows double-pulse LIBS to be applied to energetic material detection with great effect. When the first pulse hits, it impacts the sample and displaces the surrounding gas. The second pulse arrives and interacts with the material within the first plasma. Therefore, the influence from atmospheric oxygen and nitrogen will be decreased. In the case of RDX, the oxygen-to-nitrogen ratio should increase from single-pulse to double-pulse LIBS. In figure 11, the oxygen and nitrogen region (~725–800 nm) from a double-pulse LIBS spectrum of RDX and a single-pulse LIBS spectrum of RDX is compared. The oxygen-to-nitrogen peak intensity ratio is larger for the double-pulse spectrum. The double-pulse method may prove effective for utilizing standoff LIBS for explosives detection. The standoff system developed for ARL has double-pulse capability. The LIBS spectrum in figure 10 is collected from a plasma generated by a double-pulse laser at a standoff distance of 20 m.

Another method that could be employed for standoff LIBS is using femtosecond lasers. Traditionally, LIBS is performed with nanosecond laser pulses. Femtosecond pulses have been shown to have advantages over nanosecond pulses for LIBS applications (*89–91*). Most importantly, because of the shorter time (~10^{-15} s vs. 10^{-9} s), all of the energy is deposited into the sample and not the surrounding atmosphere. With the longer pulse, the tail end of the laser
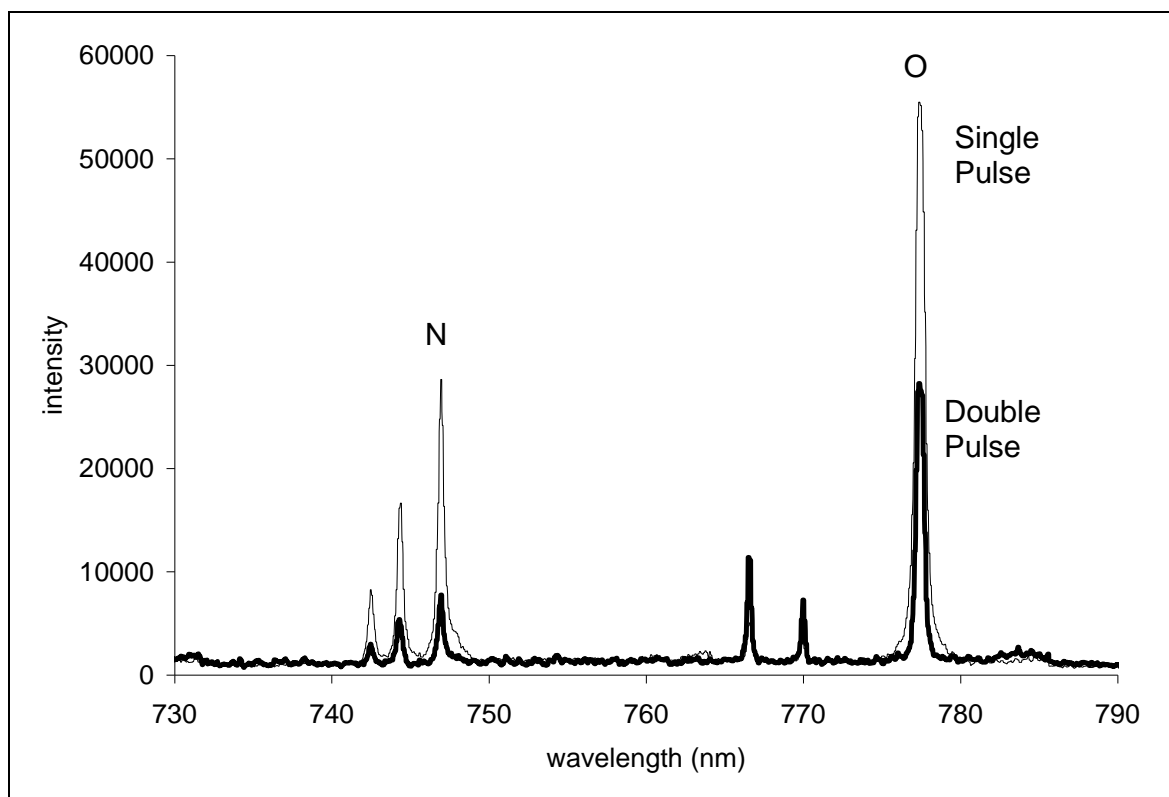
Figure 11. Comparison of LIBS spectra of RDX using the double-pulse configuration and the single-pulse configuration. Two 160-mJ pulses were separated by 2 μs for the double-pulse spectrum. One 320-mJ pulse was used to collect the single-pulse spectrum. The O-to-N intensity ratio for the double pulse and single pulse is 4 and 2, respectively.

reheats the plasma, thus leading to the air entrainment within the plasma and contributing to oxygen and nitrogen signal. The femtosecond pulse only deposits energy into the sample, thus minimizing the oxygen and nitrogen from the atmosphere. Femtosecond LIBS for explosives detection is in the beginning stages (*92*). As femtosecond lasers become more mature, performing femtosecond LIBS in the field becomes more plausible. More fundamental studies will be needed in the laboratory in order to achieve better understanding of the femtosecond pulse material interaction for LIBS.

3.4 LIBS Summary

To make explosives detection more reliable, there are concerns with LIBS that still need to be overcome. As previously mentioned, interference from atmospheric oxygen and nitrogen is a problem when trying to detect explosives. In addition, the plasma also samples everything around the explosive, such as the surface material an explosive rests on as well as any environmental contamination, i.e., dust, oil. Designing systems that can preferentially sample a residue can help eliminate surrounding interference. Double-pulse LIBS minimizes the contribution from the surrounding atmosphere. In addition, appropriate wavelength selection may allow more absorption of the laser energy into the residue as opposed to the underlying

surface. For the standoff application, eye safety is a concern. One way to alleviate this problem is to use eye-safe laser wavelengths, such as 1.5 µm. The laser power at the focus can still cause eye damage, but the majority of the laser path length and any reflections of the beam will be in the eye-safe region. The LIBS technique also suffers from poor reproducibility and sensitivity. The poor reproducibility can be caused by a number of things, including pulse-to-pulse variability, differences in the laser coupling with the sample, and sample heterogeneity. Some of these issues can be solved by using lasers with better pulse-to-pulse uniformity or even femtosecond pulses which have been shown to increase reproducibility (*89–91*). While LIBS has been shown to be able to detect explosives residues, the limit of detection has not yet been established. In general, most limits of detection are around ppm. However, this is highly dependent on the surrounding environment. There are several things that can be done to enhance the LIBS signal. The double-pulse method and/or using femtosecond pulses have been shown to increase light intensity. Also, more efficient spectrometers and detectors are being developed to maximize light collection. Even with these issues still in need of resolution, LIBS has many advantages as an explosive detection technique. The ability to design field ready instruments is a major advantage. Unlike most explosive detection techniques that rely on the detection of trace explosive vapors (RDX is typically in the ppt range) or extensive sample preparation procedures, LIBS requires no sample preparation and can perform analysis on solid samples, making it extremely attractive as an explosives detector in the field. Since there is no sample preparation, there is no waste or cost generated by consumables. In addition, a spectrum can be collected in real time, allowing instantaneous detection of a potential threat. The simple components allow different types of system configurations, leading to development of man-portable systems for point detection or larger standoff systems for detecting explosives at a distance. These attributes make the use of LIBS for explosives detection a promising technique.

4. Terahertz Spectroscopy

4.1 Introduction

The terahertz (THz) region, generally accepted to span 0.1 to 10 THz, falls between the infrared and microwave regions of the electromagnetic spectrum (*93*). Long considered a tool for the study of small molecules by astronomers and chemists, THz spectroscopy has recently (in the last decade) found itself the subject of intense research interest (*94*). This explosive growth in THz spectroscopy has been driven by the development of more efficient THz emitters and detectors, new detection schemes such as terahertz time-domain spectroscopy (THz-TDS), and the need for new methods to address many challenging problems in the fields of industry, medicine, and homeland security.

This section focuses on studies performed using THz-TDS spectroscopy and imaging for explosives detection. While other means of THz wave generation and detection exist, the most current research in this field utilizes this time-domain technique. For more information on the scope of THz spectroscopy fundamentals and applications, the reader is referred to several books and reviews (*95–99*).

4.1.1 THz-TDS

THz-TDS developed from studies performed by ATT and IBM to detect ultra-short electronic pulses in transmission lines (*100–102*). A typical THz-TDS system is composed of an ultra-fast laser, emission and detection photoconductive antennas, an optical delay line, and assorted optics to guide and focus the laser and THz emission. Figure 12 depicts a standard THz-TDS system. In this system, the mode-locked output of a titanium sapphire laser (100 fs, 800 nm) is first split by a beam splitter. One portion of the emission illuminates a photoconductive antenna (typically, GaAs) producing sub-ps pulses of THz radiation. The resulting THz radiation is collimated, focused into free space using an off-axis parabolic reflector, and directed onto a second photoconductive antenna (detector) with a second parabolic mirror. The second portion of the titanium sapphire laser output passes through an optical delay line and impinges on the detection antenna. The wave form of the generated THz field is measured by scanning the optical delay line (*98, 103*). Systems constructed in this manner typically produce broadband radiation from ~100 GHz to 2 or 3 THz (*104*). Sample measurement is facilitated by placing a sample in the THz beam path and measuring the time-dependent wave forms with and without the sample. The resulting wave forms are Fourier transformed to obtain the frequency dependent amplitude and phase shift. These amplitude and phase shift values can then be used in an iterative manner to obtain the transmittance and refractive index values at each frequency (*103, 105*).

In addition to measuring transmission, THz-TDS may also be performed using THz reflected from the sample surface. Performance of a reflection study requires the exact placement of a mirror at the sample position for the blank measurement. Incorrect placement causes inaccuracy in the measurement of the frequency-dependent phase shift (*106*).

4.1.2 Advantages and Limitations of THz-TDS

THz-TDS possesses several advantages, making it useful for a host of applications (see section 4.1.3). THz radiation is measured coherently, providing high sensitivity and time-resolved phase information (*96*). Time resolution and gating minimizes influence of background thermal radiation (*103*). Consequently, THz-TDS systems operate against fundamental limits like the shot noise of the detector. These systems typically exhibit signal-to-noise ratios on the order of 60 to 100 dB (*107*). Each THz-TDS measurement yields both the electric field intensity and phase shift associated with the sample being measured. The wave form amplitude and phase shift are directly related to the absorption (or reflection) coefficient and refractive index of the sample. Because amplitude and phase shift are obtained in a single measurement, no Kramers-Kronig analysis is needed to obtain the refractive index (*102, 103*).
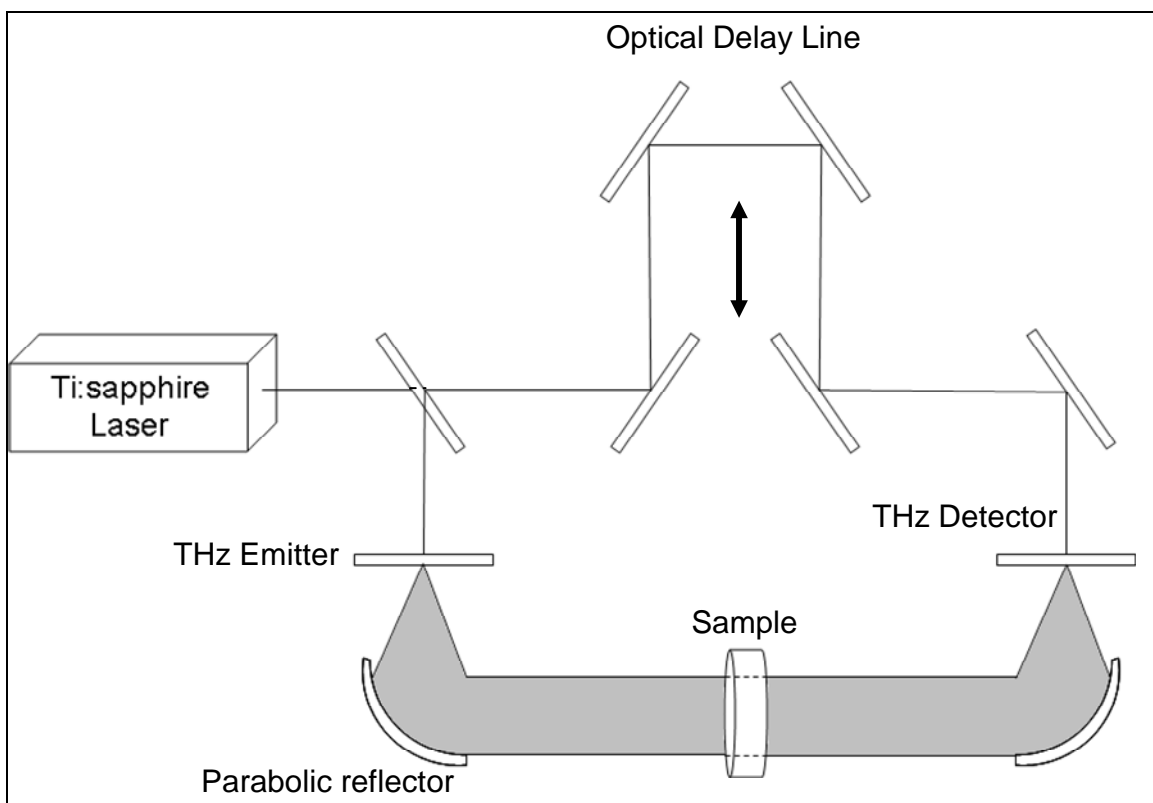
Figure 12. Instrument diagram of a typical THz-TDS system. In this configuration, sample transmission is being measured.

The characteristic signatures of many materials can be detected using THz-TDS (*108*). Spectroscopy in the THz domain probes many inter- and intramolecular vibrations—rotational modes, van der Wal forces, internal macromolecular vibrational modes, twisting, bending and stretching modes around hydrogen bonds in dimmers and trimmers, lattice vibrations, isomeric and polymorphic configurations (*93*, *107*, *109*). Pump-probe spectroscopic measurements can easily be performed by modifying a standard THz-TDS setup. The probe pulse can be generated with the same laser used to create the THz pulses with a time delay (*103*).

Imaging using THz energy was first demonstrated by Hu and Nuss in the mid-nineties (*110*). Since then, many others have recognized the potential industrial, medicinal, and security application of THz-TDS imaging (*108*, *111*, *112*). THz radiation is readily transmitted through most nonmetallic and nonpolar materials such as plastics, ceramics, clothing, paper, dust, and sand (*107*, *108*). The THz transmission characteristics of several materials that might be encountered in security applications are shown in table 2. Unlike x-ray imaging, THz radiation is nonionizing and can be used at low power levels (*108*). Images using THz radiation can be obtained with reasonable speed and high resolution. Imaging systems that can collect THz waveforms at rates up to 4 kHz and can raster scan at rates up to 100 Hz have been demonstrated (*107*). Because THz-TDS emitters are point sources, THz radiation can be focused to nearly diffraction limited size (*103*). As a result, THz images can be obtained in high resolution.

22

Table 2. THz transmissive properties of common materials encountered during security screenings. N, the number of layers, indicates the number of layers that result in a signal-to-noise ratio of 1.

Material	Trans (%)	N (Layers)	Trans. % @ 1.0 THz	Trans. % @ 0.5 THz
Leather glove[a]	4	3	2.8	3.2
Coat	14.7	6	3.8	22.8
T-shirt	87.5	86	70.6	87.4
Sweater	21.6	7	1.9	40.8
Sock[a]	26.7	8	13.2	35.5
Wallet	9	4	0.6	18.3
Laptop bag[a]	3	3	0.8	4.1
Cardboard	62.5	24	9.2	53.7
Carpet	56.7	20	0.3	35.5
Bubble plastic	91.1	128	84.0	95.1

[a]The entire item was measured instead of just one layer. Used with permission from Xu et al. (*113*).

The greatest strength of THz-TDS comes from the marriage of imaging and spectroscopic material characterization. This fusion of imaging and material signatures forms the basis of many proposed applications of THz-TDS, including explosives screening and detection.

While having many advantages makes it a potential attractive solution for many real-world problems, THz-TDS has several disadvantages which may ultimately limit its application. THz-TDS has a coarser resolution than techniques using narrowband THz sources (e.g., QC lasers) and a smaller spectral range than infrared FT spectroscopy (*96*). THz absorption line widths can vary with sample and local environment (i.e., matrix effects). Consequently, instrumentation and operational parameters may be specific to each application (*93*).

The major disadvantage of THz techniques arises in applications requiring THz wave propagation through the atmosphere. Several groups have studied the absorbance of THz radiation by water vapor (*114*, *115*). Water exhibits strong absorption lines in nearly all of its rotational modes. The frequency range of 0.1 to 1 THz contains over 228 individual spectral lines for water vapor (*93*, *107*). In a study performed by Yuan et al. (*115*), THz radiation from a THz-TDS system was studied as a function of relative humidity (3%–100% humidity, frequency range 0–2 THz). As relative humidity was increased, a drop in the peak THz frequency value was observed, along with the appearance of water vapor absorption lines. Above 1 THz, many water absorption lines were observed, and the THz amplitude decreased with increasing humidity. Below 1 THz, less water absorption lines were observed, and the THz drop in amplitude around these lines was smaller. In addition to atmospheric water vapor, other atmospheric species can add to the observed spectral background. These species may include gaseous species such as O_2, CO, CO_2 O_3, N_2O, and CH_4, as well as small suspended particulates, especially particulates whose size approaches the wavelength of the THz radiation (*93*).

23

THz-TDS systems have been used to study a range of materials such as polymers, semiconductors, and biological and pharmaceutical preparations. Of great interest to many is the development of security-based applications using THz-TDS spectroscopy and imaging. Coupling the ability to image through objects with the identification power of spectroscopy has lent researchers to suggest many potential security applications—screening of individuals (*108*, *116*), luggage and packages, and ships and shipping containers (*117*). In addition to the detection of hidden knives and personal firearms, THz-TDS has been proposed as a method to detect and identify other concealed materials such as biological and chemical warfare agents, weapons of mass destruction, and explosives (*107*, *118–121*).

4.2 THz Spectroscopy and Imaging of Energetic Materials

Explosives studies using THz-TDS fall into two basic categories: (1) fundamental spectroscopic and theoretical modeling studies of explosive spectral signatures and (2) proposed applications for explosives and explosive device detection. The majority of research efforts to date illustrate that characteristic spectra of explosive materials may be obtained using THz-TDS. The application of explosive detection to real security applications—such as mail and package, container, landmine detection, and standoff detection—remains relatively unexplored, with a few "proof of principle" type experiments demonstrating the potential of these techniques.

4.2.1 Fundamental Spectroscopy and Theoretical Calculation of Explosive Molecules in the THz Region

THz spectroscopy of energetic materials has been demonstrated by several different research groups. The objective of many of these works is to identify THz spectral features suitable for explosives identification. A summary of energetics studied, prominent spectral features, sample preparation methods, and the data collection method is presented in table 3. Each of these materials between 0 and 4 THz exhibits several characteristic absorbance peaks suitable for identification. Furthermore, reasonable agreement in energetic spectral features is also observed between independent research groups. For example, Lo et al. identified seven absorbance peaks for 1,3,5-trinitro-s-triazine (RDX) ranging from 0.81 THz to 3.09 THz (*122*). Comparison of RDX spectral features results from several groups suggest that identifying RDX might be based on spectral features at 0.81, 1.05, and 1.35 THz. Examples of energetic material absorbance spectra are shown in figure 13. While much agreement is clearly seen between measurements made by independent groups (see table 3), discrepancies in observed THz spectra of energetic material do occur. These differences may be attributed to several factors such as sample preparation method (e.g., pressed pellet and pellet with matrix), sample impurities, or the experimental configuration used (e.g., transmission or reflectance and inert atmosphere or open air).

Mixtures of explosives with other explosives or filling materials (as occurs with operational explosives such as C-4) retain these characteristic energetic material THz absorption spectral features. Semtex-H, a mixture of RDX and a second explosive (PETN) yields THz absorption spectra with features indicative of both explosive components.

Table 3. Summary of energetic and simulant materials spectral features observed using THz spectroscopy.

Material	Peaks in THz	Method	Preparation	Source
2,4-dinitrotoluene	1.08	t	Pellet	(*123*)
	≈0.25, ≈1.2	t	Thin film on Si wafer	(*124*)
C-4 (RDX + plasticizer)	0.81,1.1,1.36,1.53,1.97,2.24	t	Pellet	(*125*)
	0.81,1.1,1.36,1.53,1.97	t	Pellet in paper envelope	(*125*)
Dinitrobenzene	≈0.18	t	Thin film on Si wafer	(*124*)
HMX	1.58,1.91,2.21,2.57	t	Pellet	(*120*)
	1.84	t	Pellet	(*126*)
	1.77,2.46,2.85	t	Pellet	(*122*)
Metabel (PETN-based)	2.04,2.16,2.91	t	Bulk material	(*122*)
	2.00,2.88	r	Bulk material	(*122*)
Ammonium nitrate	Monotonically increasing spectrum	t	Pellet	(*126*)
PBX 9501 (95% HMX)	No peaks listed	t	Bulk material	(*127*)
PBX 9502 (95% TATB)	No peaks listed	t	Bulk material	(*127*)
PE4 (RDX + Plasticizer)	0.72,1.29,1.73,1.94,2.21,2.48,2.69	t	Pellet	(*120*)
PETN	1.73,2.51	t	Pellet	(*120*)
	2.01	t	Pellet	(*126*)
	≈2.1	t	Pellet	(*128*)
	≈2.1	t	Mixed in vacuum grease	(*128*)
	1.86,2.16,2.88	t	Pellet	(*122*)
RDX	0.72,1.26,1.73	t	Pellet	(*120*)
	0.82,1.05,1.35,1.55	r	Pellet	(*129*)
	0.81	t	Pellet	(*126*)
	≈0.79	t	Pellet	(*128*)
	≈0.80	t	Mixed in vacuum grease	(*128*)
	0.79,1.05,1.34,1.44,1.56,1.77,1.92	t	Pellet	(*130*)
	0.82,1.05,1.38,1.55,1.96,2.22,3.16	t	Pellet	(*131*)
	0.82	r	Bulk material	(*131*)
	0.81,1.05,1.38,1.53,1.98,2.22,3.09	t	Pellet	(*122*)
Semtex-H (RDX+PETN)	0.81,1.05,1.38,1.53,2.04,3.00	t	Bulk material	(*122*)
	0.81,2.00,2.88	r	Bulk material	(*122*)
	0.72,1.29,1.73,1.88,2.15,2.45,2.57	t	Pellet	(*120*)
	0.8,1.05,1.4	r	Bulk material	(*116*)
SX2(RDX-based)	0.81,1.05,1.38,1.53,1.98,2.22,3.06	t	Bulk material	(*122*)
	0.81	r	Pellet	(*122*)
	0.8,1.05,1.4	r	Bulk material	(*116*)
TNT	1.44,1.91	t	Pellet	(*120*)
	1.7	t	Pellet	(*126*)
	1.59,2.19,3.81	t	Pellet	(*122*)

Notes: • This list should not be considered all inclusive.
  • SX2 = RDX-based sheet explosive.
  • "Method" indicates whether the measurement was t – transmission or r – reflectance.
  • "Preparation" indicates the type of sample studied.
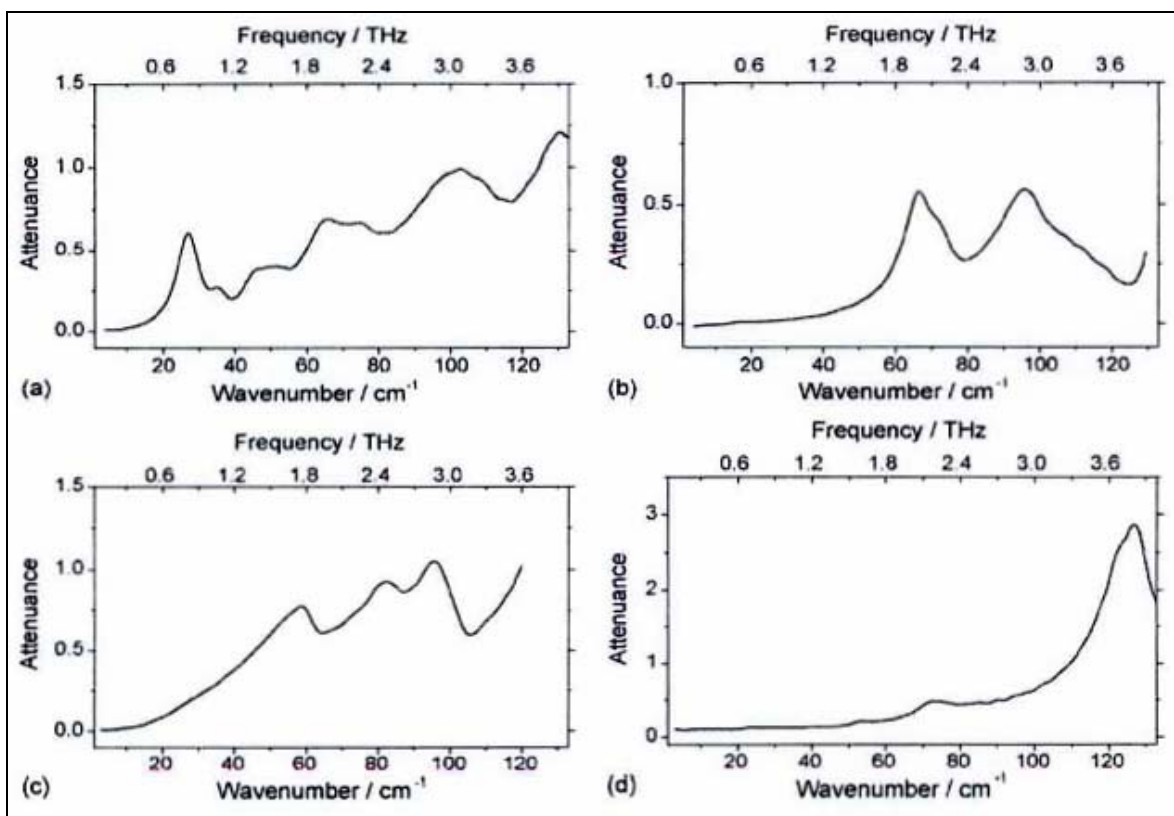
Note: Reprinted from Lo et al. (*122*) with permission from Elsevier.

Figure 13. THz-TDS spectra of several explosive samples – (a) RDX, (b) PETN, (c) HMX, and (d) TNT.

RDX features at 0.81 and 1.05 THz and PETN features at 2.00 and 2.88 THz are observed (*120*). C-4, a mixture of RDX and plasticizer, retains many of the spectral features found in pure RDX (*125*). Example spectra of several mixtures are displayed in figure 14.

THz-TDS absorbance spectra of confusant materials—substances that might be mistaken for explosives in a screening application—have also been collected. Common gel-like baggage items were studied (*122*). Items included various foods (mustard, cheese, jam, honey, margarine, peanut butter, and chocolate spread), sucrose, and toiletries (hair gel, liquid soap, and toothpaste). THz absorbance spectra of most of these materials exhibited broad THz spectra with no distinguishable spectral features. The exception, chocolate spread, exhibited several sharp spectral features originating from sucrose in the sample. Each explosive investigated in this study was distinguishable from the confusant materials by its THz absorbance spectrum.

The feasibility of using THz spectroscopy to identify explosives concealed in envelopes has been demonstrated by Yamamoto et al. (*125*). In this work, THz absorption spectra were acquired from THz radiation transmitted through a sealed envelope containing a piece of C-4 several millimeters thick. A difference spectrum was generated from spectra of the sealed envelope containing C-4 and an empty envelope. This difference spectrum was shown to exhibit the same spectral features as a pure C-4 spectrum. The authors note that while being able to identify the
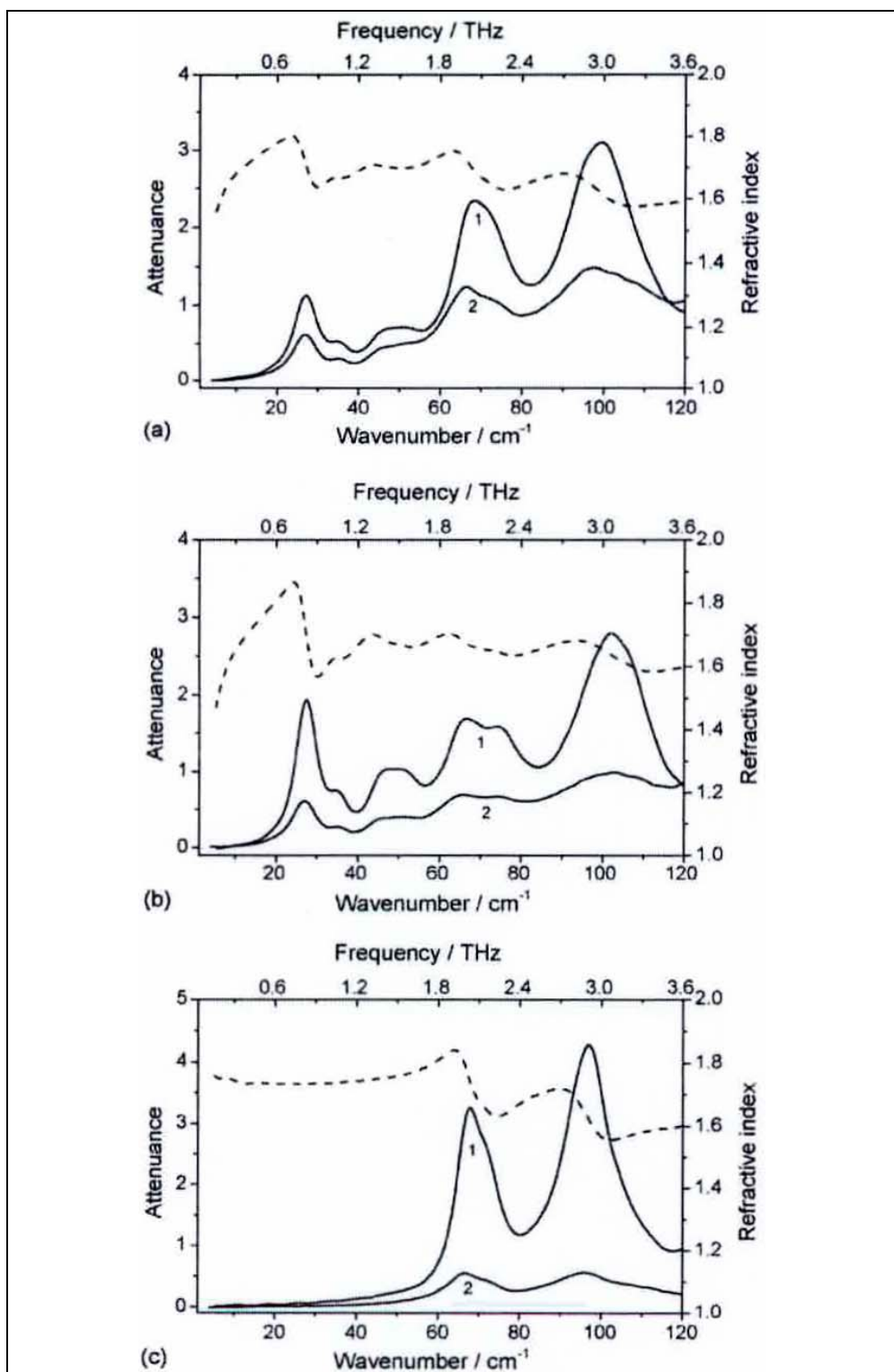
Note: Reprinted from Lo et al. (*122*) with permission from Elsevier.

Figure 14. THz absorbance spectra of plastic and sheet explosives (explosive mixtures).
(a) 1 = Semtex H; 2 = composite spectrum of RDX and PETN, (b) 1 = SX2,
2 = RDX, and (c) 1 = Metabel, 2 = PETN. Note the similarity in spectral features
between the explosive mixtures (1) and their pure components (2).

presence of the explosive, this technique is limited to samples several millimeters thick due to absorption of THz radiation by the sample.

In support of fundamental spectroscopic studies, molecular calculations and modeling have been performed on explosive molecules to explain the origin of observed peaks in the far infrared and THz regions. Most of these studies have focused on the far infrared regions where intramolecular vibrational modes dominate. In these studies, explosive molecules are typically modeled as single molecules with no environmental interactions. Explosive species such as HMX (*132*), PETN (*133*), and RDX (*134*), as well as explosive simulants such as 2,4-dinitrotoluene (*123*), have been modeled using these isolated molecule approaches. As previously mentioned, transitions within the THz region typically originate from intermolecular vibrations and phonon modes. Consequently, more accurate modeling of transitions within the THz region requires the addition of periodic boundary conditions to the model.

An example of the predictive power of including the crystal environment in density functional calculations of the explosive HMX has been demonstrated recently by a group at Syracuse University (*135*). Molecular calculations of HMX using periodic boundary conditions were performed and compared to experimentally derived results. Experimental measurements of HMX yielded three HMX spectral features at 1.75, 2.46, and 2.86 THz. Similar features were observed at 1.76, 2.50, and 2.86 THz using solid-state calculation methods. The authors assigned these features to two optical rotational modes (molecules in the crystal cell spin clockwise about their axis of rotation) and an antisymmetric ring twisting motion.

4.2.2 Application of THz-TDS Imaging to Explosives Detection

As previously discussed, the combination of imaging with THz spectroscopy has the potential to be a powerful technique for many applications such as explosives detection or screening. To date, several studies have been performed demonstrating the concept of imaging applied to the identification of concealed explosives. The technique, however, still has many challenges to be overcome such as spectral noise, effects of concealing materials (e.g., multiple internal reflections and strong absorption), similarities in THz spectra, and atmospheric humidity absorption (*119*). Investigation of computational methods, such as neural networks, and advanced image processing to address some of these challenges has been performed (*119, 136, 137*).

The ability to image and discriminate explosives from several different materials has been demonstrated by Shen et al. (*131*). In this work, pellets of lactose, sucrose, and RDX were imaged by reflection of a THz beam raster scanned across each pellet surface (figure 15a). Regions of high contrast were observed for the sucrose and RDX. The authors attribute these regions of contrast to large particles present in the sucrose sample and the roughness of the RDX sample surface. For identification purposes, a THz absorbance spectrum of each imaged pixel was calculated and compared against a matrix composed of known explosive THz spectra, and the image was reconstructed. In this image, bright pixels indicated the presence of the explosive RDX (figure 15b).
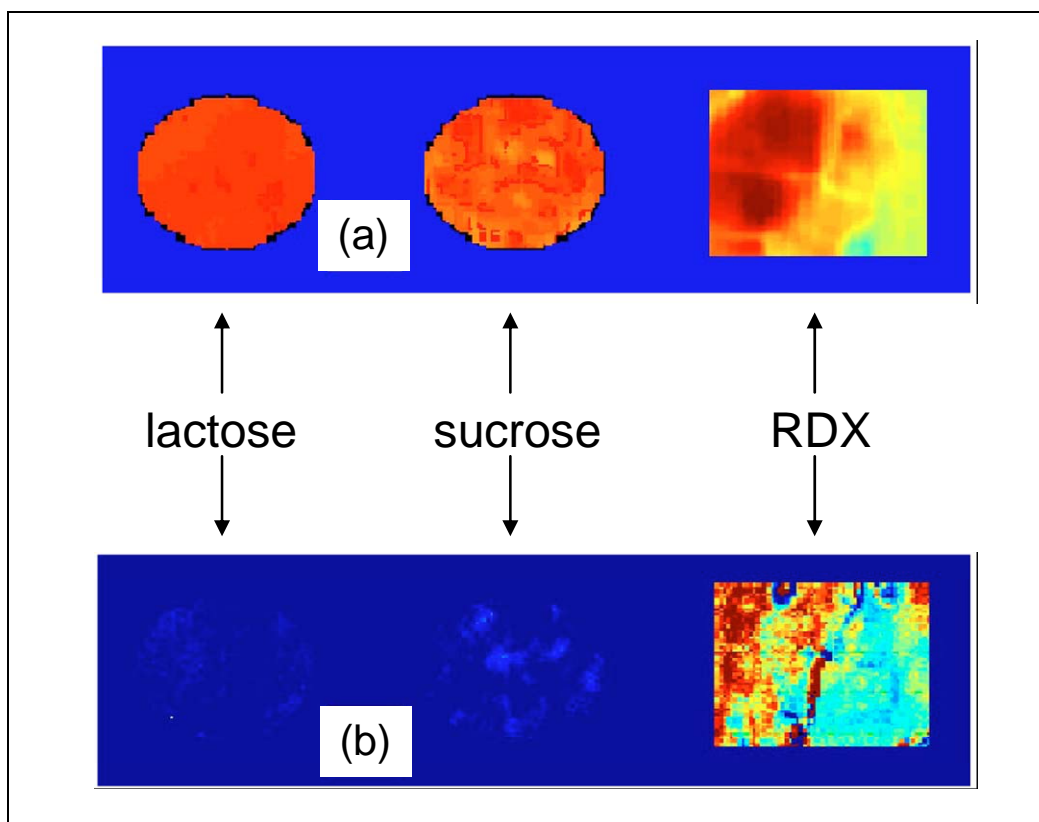
Figure 15. (a) False color THz images of chemical spatial distributions of (from left to right)
lactose, sucrose, and RDX. (b) Identification of RDX after imaging processing
algorithms, which match samples against a library of known materials.

THz imaging applied to personal screening has been studied. Using a prototype hand-held wand, researchers from TeraView demonstrated the imaging of SX2 hidden behind several layers of leather worn by a human subject (*116*). The SX2 was observed as discontinuity in the image against the skin of the test subject. No spectral identification of the explosive hidden on the individual was performed. Continuing efforts in the development of computer algorithms for hidden object and spectral identification are mentioned.

In addition to direct detection of explosives, imaging with THz-TDS has been proposed as a means for detecting hidden explosive devices. Buried landmines in war-torn regions of the world continue to claim victims. The detection of these buried devices is a risky, difficult task. Recent studies have been performed illustrating the applicability of THz-TDS to landmine detection (*124*). In this work, the ability to image a buried target as a function of soil depth and water content was studied. Preliminary studies were preformed to determine the attenuation of THz radiation due to sand thickness and humidity content. In a sample composed of dry sand 1.27 cm thick, frequency-dependent attenuation of THz radiation was observed with attenuation of ~5 dB/cm at 100 GHz and 22 dB/cm at 350 GHz. Measured attenuation was found to be

similar to Mie scattering observed for particle sizes around 100 μm. Adding water—dry to 2.5% by weight—resulted in an order of magnitude loss in THz peak amplitude or an attenuation of 8.2 dB/cm%. Following this preliminary work, a neoprene grommet was placed 1.2 cm deep in the sample holder containing dry sand. THz absorption images were collected in a transmission configuration. The resulting image of the grommet was identifiable as a ring shaped object; however, the image contrast was extremely poor due to scattering by the soil matrix. The authors suggest that based on the current performance of THz instrumentation (80 dB signal-to-noise ratio) and their experimental results, visualization into soil depths of 6 cm and 1% humidity should be possible.

4.2.3 Standoff Detection of Explosives Using THz Spectroscopy

Ideally, an explosives detection system should be able to detect the explosive material while the operator remains protected from explosive detonation. In practice, this is performed two ways: (1) remote operation of a detection system, such as a robotic platform that takes the equipment to a suspected hazard or (2) a standoff detection system in which the equipment and operator query suspect explosives from a safe distance. Standoff detection is typically preferred because equipment losses in the event of a detonation are substantially lower.

Many challenges face the development of a standoff THz-TDS system. In order to perform standoff, the THz beam must first be propagated through the atmosphere. As previously mentioned, THz radiation may be strongly attenuated from many things in the atmosphere—water vapor, simple gases, and airborne particulate matter (*93*, *114*, *115*). Typical losses to the atmosphere of 50 dB km^{-1} at 0.8 THz have been reported (*119*). Attenuation losses will also occur from passing through material layers concealing explosives. These losses are dependent on the physical nature and thickness of the material covering the target. Furthermore, detection of THz radiation for standoff applications is best suited to reflection measurements. The majority of explosive studies to date have been transmission-type measurements.

Despite these challenges, several groups have explored THz-TDS standoff explosives detection. In work performed by a group from TeraView (Cambridge, UK), reflective spectra of explosive samples SX2 (>80% RDX by volume) and Semtex-H (~40% RDX by volume) were collected at a standoff distance of 1 m (2 m total light path) (*116*). Spectra were real-time processed to remove water vapor absorption lines. Collected spectra compared with calculated spectra obtained from transmission measurements yielded similar results. In an extension of this study, the authors collected a spectra of explosives at a 1-m standoff distance behind layers of clothing material. While the addition of clothing layers attenuated the signal, the authors were still able to resolve the 0.8-THz feature of the RDX in SX2 behind four clothing layers by examining the derivative spectrum.

In a second study, Liu et al. measured the reflectance of RDX behind different materials—paper, polyethylene, leather, and polyester (*129*). These spectra were collected in open atmosphere and with a 1.1-m THz path (equivalent to a standoff distance of about 0.5 m).

The authors reported problems with attenuation due to water absorption, especially above 1.0 THz. Barrier materials were shown to distort the observed spectra; however, the 0.82-THz peak of RDX remained clearly visible.

The distance limits of standoff detection of explosives have recently been studied by H. Zhong of Rensselaer Polytechnic Institute (*138*). Using THz-TDS, generated THz radiation was propagated through the atmosphere and focused by parabolic mirrors onto an RDX sample. Absorption spectra were collected by reflectance at distances of 2.5, 10, 20, and 30 m from the sample. Despite broadening of spectral features and increased water line intensities due to long atmospheric propagation distances, the RDX absorption peak at 0.82 THz was still visible (but broadened) at 30 m.

4.3 Conclusions

THz-TDS exhibits strong potential as a means of detecting explosive materials. To date, significant efforts have been made in trying to understand the interaction of THz radiation with explosive materials and to characterize their spectra. The marriage of spectral identification with imaging provides even stronger arguments for using this technology as a means to detect concealed explosives and explosive devices. Despite these powerful features, the practical application of THz-TDS in screening-type applications is still in its infancy. Simple demonstrations of imaging and spectral characterization of energetic materials have been performed, but typically only in laboratory conditions, and not in realistic operational environments. Standoff detection of the explosive RDX has been demonstrated to 30 m in a laboratory setting. Current research initiatives have demonstrated the principle of explosives imaging and identification; however, much testing and many refinements are still required—such as improved detection technologies and spectral and image analysis methods and the development of lower-cost THz equipment—before THz detection of explosives in the field becomes feasible.

5. Other Laser-Based Methods for Explosives Detection

In addition to the IR/Raman, LIBS, and THz imaging methods previously discussed, a number of other laser-based methods for explosives detection have been developed over the years. The following section briefly describes the ultraviolet visible spectroscopy (UV/Vis) absorption spectra of energetic materials and discusses the techniques of laser desorption, photofragmentation with detection via resonance-enhanced multiphoton ionization (REMPI) or laser-induced fluorescence (LIF), photoacoustic spectroscopy (PAS), variations on the LIDAR method, and photoluminescence. Table 4 lists the limits of detection (LOD) of several explosive-related compounds (ERC) and energetic materials (EM) obtained by the techniques described in this section.

Table 4. Detection limits for ERCs and EMs. LODs for several studies were not determined.

EM/ERC	Technique	Reference	Phase	LOD
Nitroglycerin (NG)	PAS, 6 μm, 9 μm, and 11 μm	(139)	Vapor	0.28 ppb
	PAS, 9.6 μm	(140)	Vapor	0.23 ppb
Nitrobenzene (NB)	REMPI/TOF, 226.3 nm	(141)	Vapor	Subattomole
	REMPI/TOF, 226 nm (100 °C)	(142)	Vapor	2.4 ppm
	PF-REMPI, 193 nm	(143)	Vapor	0.49 ppm
	LP-LIF, 222–272 nm (10–100 Torr air)	(144)	Vapor	~500 ppb
	SPI-TOF-MS, 118.2 nm	(145)	Vapor	17-24 ppb
Dinitrobenzene (DNB)	LP-LIF, 248 nm (100 Torr, 500 Torr air)	(146)	Vapor	11-13 ppb
Ethylene glycol dinitrate (EGDN)	PAS, 6 μm, 9 μm, and 11 μm	(139)	Vapor	1.5 ppm
	PAS, 9.6 μm	(140)	Vapor	8.26 ppb
Hexahydro-1,3,5-trinitro-s-trazine (RDX)	IRMPD-LIF, CO_2 laser + 280 nm (150 °C)	(147)	Vapor	—
	REMPI/TOF, 226 nm (100 °C)	(142)	Vapor	8 ppb
	PF-REMPI (with electrodes), 227 nm (1 atm, air)	(148)	Vapor	7 ppb
	SPF-REMPI, 248 nm + 226 nm (1 atm, 298 K)	(149)	Solid	~14 ng/cm^2
	PF-LIF, 227 nm (1 atm, air)	(148)	Vapor	ND
	Pyrolysis-LIF, 227 nm (1 atm, air)	(148)	Vapor	~1.6 ppm
	PAS, 5.8–6.7 μm	(150)	Vapor	~ppb
	PAS, 9.6 μm, 10.6 μm	(151)	Solid	—
Octahydro-1,3,5,7-tetrocine (HMX)	IRMPD-LIF, CO_2 laser + 280 nm (180 °C)	(147)	Vapor	
Nitrotoluene (NT)	R2PI, 266 nm (1 atm, He)	(152)	Vapor	—
	R2PI, 213 nm (1 atm, He)	(152)	Vapor	—
	PF-REMPI, 193 nm	(143)	Vapor	0.10-0.12 ppm
	PF-REMPI, 226 nm	(143)	Vapor	15-36 ppm
DNT	UV CRDS	(153)	Vapor	<1 ppb
	R2PI, 266 nm (1 atm, He)	(152)	Vapor	ND
	R2PI, 213 nm (1 atm, He)	(152)	Vapor	—
	LP-LIF, 248 nm (100 Torr, 500 Torr air)	(154)	Vapor	2.7-3.7 ppb
	SPI-TOF-MS, 118.2 nm	(145)	Vapor	~40 ppb
	PAS, 5.8–6.7 μm	(150)	Vapor	~ppb
	PAS, 6 μm, 9 μm, and 11 μm	(139)	Vapor	16 ppm
	PAS, 9.6 μm	(140)	Vapor	0.50 ppb
Trinitrotoluene	UV CRDS	(155)	Vapor	<1 ppb
	R2PI, 266 nm (1 atm, He)	(152)	Vapor	ND
	REMPI/TOF, 226 nm (100 °C)	(142)	Vapor	24 ppb
	PF-REMPI, 193 nm	(143)	Vapor	0.21 ppm
	PF-REMPI, 226 nm	(143)	Vapor	1.7 ppm
	PF-REMPI (with electrodes), 227 nm (1 atm, air)	(148)	Vapor	70 ppb
	LIF, 226 nm	(156)	Vapor	~40 ppb
	LIF (2 μJ, 473 K), 226 nm	(157)	Vapor	4 ppm
	PF-LIF (1 atm, air)	(148)	Vapor	37 ppm
	PF-LIF, 248 nm (24 °C, 1 atm air, 15 cm)	(158)	Vapor	<8 ppb
	PF-LIF, 248 nm (28 °C, 1 atm air, 2.5 m)	(159)	Vapor	<15 ppb
	PAS, 5.8–6.7 μm	(150)	Vapor	~ppb
	PAS, 9.6 μm, 10.6 μm	(151)	Solid	—
	Fluorescence LIDAR (close contact)	(160)	Aqueous	1 ppm
	Fluorescence LIDAR (500 m)	(160)	Aqueous	100 ppm

Table 4. Detection limits for ERCs and EMs. LODs for several studies were not determined (continued).

EM/ERC	Technique	Reference	Phase	LOD
PETN	PF-REMPI (with electrodes), 227 nm (1 atm, air)	(*148*)	Vapor	2 ppb
	PF-REMPI (with electrodes), 454 nm (1 atm, air)	(*148*)	Vapor	16 ppm
	PF-LIF, 227 nm (1 atm, air)	(*148*)	Vapor	ND
	PF-LIF (with pyrolysis), 227 nm (1 atm, air)	(*148*)	Vapor	2.2 ppm
	PF-LIF (with pyrolysis), 454 nm (1 atm, air)	(*148*)	Vapor	140 ppm
	PAS, 5.8–6.7 µm	(*150*)	Vapor	~ppb
TATP	LP-TOF-MS, 795 nm (130 fs, 840 µJ, 298 K)	(*161*)	Vapor	—
	LP-TOF-MS, 266 nm (5 ns, 30 mJ, 298 K)	(*161*)	Vapor	—

Notes: • For definitions of the acroynyms in this table, please refer to the List of Symbols, Abbreviations, and Acronyms.
 • ND in the table indicates non-detection of the material.

5.1 UV/Vis Absorption

Typically, the absorption spectra of energetic materials are obtained in order to determine the optimal wavelength for laser ignition with the minimal pulse energy. When attempting to selectively ablate an explosive residue on the surface of a substrate for LIBS detection, the ablation laser should ideally be at a wavelength that is efficiently absorbed by the explosive; otherwise, the laser energy passes through the residue and is absorbed by the substrate. In order to determine the most desirable laser wavelength for trace residue detection, the broadband absorption spectra of explosives is needed. In addition to the infrared absorption spectra previously discussed (see section 2), the UV/Vis spectra of explosives have been recorded. Although most energetic materials do not absorb strongly in the visible and near-infrared regions, they do possess strong UV absorption spectra.

Smit obtained the absorption spectrum from 190–550 nm for 2,2',4,4',6,6'-hexanitrostilbene, RDX, HMX, and PETN in solution and in KCl disks (*162*). The strong absorption maxima for high explosives (HE) in the UV suggest the use of frequency quadrupled Nd:YAG lasers for LIBS detection of trace residue explosives rather than the visible or infrared wavelengths previously used (see section 3). Furthermore, laser ablation/excitation in this wavelength region reduces the laser pulse energy necessary for breakdown of the explosive sample. Not only does a lower pulse energy reduce the damage to the substrate (while still sampling all or most of the explosive residue), it becomes especially important for standoff detection, where maintaining high laser pulse energies at long distances (>100 m) could be an issue.

More recently, Usachev et al. recorded the absorption spectrum of gaseous TNT by conventional absorption spectroscopy using an Xe arc lamp as the source of UV emission (195–300 nm) as well as CRDS with a pulsed dye laser (225–235 nm) (*155*). After obtaining the broadband UV absorption spectrum, CRDS was applied to determine the real-time behavior of the TNT vapor number density at different temperatures (5–110 °C). They determined the LOD of TNT vapor by CRDS is less than 1 ppb. Ramos and Dagdigian recently presented a comprehensive study of the detection of vapors of DNBs and DNTs by UV CRDS (*153*). Their work showed that UV CRDS can detect ERCs at sub-ppb levels without any preconcentration. Unlike IR CRDS measurements,

however, measurements at atmospheric pressure result in a slight loss of detection sensitivity (5%–10%) due to Rayleigh scattering. In addition, because the UV absorption of nitro-compounds is broad and relatively structureless (see figure 16), UV/Vis absorption spectroscopy cannot provide positive identification of specific nitrocompounds. Due to the high sensitivity of the technique, UV CRDS may be useful as a screening tool supported by more selective detection techniques.
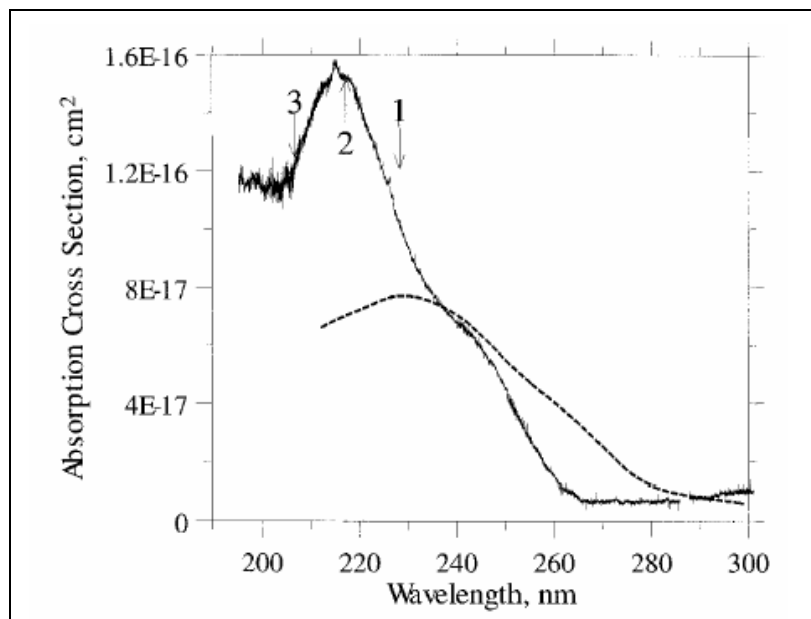
Note: Reproduced with permission from Usachev et al. (*155*).

Figure 16. The ultraviolet absorption spectrum of 2,4,6-trinitrotoluene. The solid line is the spectrum of gas-phase TNT measured at 92 °C, and the dotted line is the spectrum of the TNT ethanol solution measured in reference (*10*) of (*155*). Arrows labeled as 1, 2, and 3 show the peaks corresponding to NO $A\,^2\Sigma^+$ (v=0,1,2)←$X\,^2\Pi$(v=0) absorption transitions, respectively.

5.2   Techniques Using Laser Desorption (LD) for Sample Introduction

LD is the formation of gas-phase neutral species by the interaction of a pulsed laser with a solid or liquid material. The goal in laser desorption is to vaporize the sample material with minimal fragmentation, often as a means of sample introduction for mass spectrometry. Fragmentation reduces the selectivity of the detection technique because the vaporized fragments can no longer be uniquely identified as belonging to the parent molecule. Sample fragmentation for large, labile species such as explosives can be minimized through the use of a low-power laser or shorter pulse width.

Huang et al. (*163*) used a pulsed laser to volatilize explosive materials for ion mobility/mass spectrometry measurements. By using relatively low laser power, (532 nm, $<10^7$ W/cm^2) neutral species characteristic of the molecule were primarily produced. Ionization of the neutral species was achieved in a second step by a ^{63}Ni-β-foil atmospheric pressure ionization source or an additional laser pulse. Morgan et al. (*164*) suggested using laser thermal desorption where the infrared laser pulse serves as a source of thermal energy to increase the vapor pressure of the explosive, significantly enhancing the detection capabilities of vapor-based sensing methods. This technique provided a faster, easier alternative to heating the sample in an oven or similar device.

5.2.1 Photofragmentation-Fragment Detection (PF-FD)

Because large, fragile molecules are susceptible to nonradiative relaxation processes such as fragmentation, optical detection of energetic materials is challenging. EMs also possess relatively weak and featureless absorptions. Photofragmentation is an alternative to the direct spectroscopic approach. Characteristic fragments produced through laser photolysis of the parent molecule often prove more amenable to spectroscopic detection through their relatively sharp and strong features. Because the degree of fragmentation can be controlled by the laser fluence, different species can be identified by their fragmentation patterns (*165*). PF-FD spectrometry has received considerable attention in recent years for its ability to detect labile species such as EMs and ERCs (*166–168*). Most EMs contain one or more NO_2 functional groups, which UV excitation readily dissociates into NO (*162*, *141*, *169*). In PF-FD, one or more lasers are used to photofragment the energetic material and facilitate the detection of the characteristic NO photofragment through excitation (*148*). The NO photofragments can be monitored utilizing prompt emission excited by the photolysis, LIF, or REMPI. Detection limits are typically in the low ppb to ppm (*149*).

The first reported work on laser ionization of explosives by Marshall et al. (*170, 171*) proposed the generally accepted fragmentation mechanism of the nitro-containing explosives following excitation of the parent molecule using a nanosecond laser pulse (*145*). In the first step, the parent molecule fragments ~100 fs after initial nanosecond laser excitation, resulting in the release of NO_2 and other byproducts. NO_2 predissociates at wavelengths of <400 nm, making ionization difficult; and its weak oscillator strength and large radiative lifetime (~50–120 μs) make it difficult to detect (*142*). The NO_2 fragment absorbs additional photons and is excited to a predissociative state, resulting in the formation of NO (radiative lifetime ~200 ns) and O. Next, the NO fragment undergoes subsequent photon absorption, enabling detection of the ions and resulting from a REMPI process through the *A-X* (0–0, 0–1, or 0–2) electronic transition from the ground state $X\,^2\Pi$ to the first excited state $A\,^2\Sigma^+$ or through stimulated fluorescence emission. Subsequent studies of UV-laser (210–270 nm)-induced dissociation of nitrotoluene isomers in the gas phase concluded that dissociation ionization (dissociation followed by ionization) and ionization dissociation (ionization followed by dissociation) mechanisms are possible (*172*).

NO$_2$ absorbs in the visible region, while NO absorbs in the UV; both molecules absorb in the IR; however, few lasers can be tuned to both, and H$_2$O interference in the infrared can reduce the detection sensitivity. Therefore, detection of these characteristic fragments of explosives is usually accomplished using UV or visible wavelength lasers. Figure 17 shows a partial energy level diagram of NO$_2$ and NO, along with some of the detection schemes described in sections 5.3.1–5.4. The following sections describe photofragmentation followed by REMPI detection (PF-REMPI), photofragmentation followed by LIF (PF-LIF), and several variations of the PF-FD technique.

5.2.1.1 PF-REMPI

REMPI is a relatively efficient soft ionization technique for producing molecular ions. REMPI is based on the enhancement of the ionization process when there are electronic states resonant with the energy of one or more of the incident photons. REMPI is generally performed in a two-photon process, (1+1) REMPI, where the first photon excites the molecule to an intermediate electronic state and the absorption of a second photon results in ionization. The energy of the photons can be chosen such that ionization is induced without fragmentation. Since ionization depends on absorption of the first photon, the technique selectively ionizes the target molecules. The resulting ions are typically detected with a mass spectrometer or a pair of miniature electrodes (*173*). Efficient REMPI pathways are known for a number of species and lead to high instrumental sensitivities and low detection limits (*174*). In PF-REMPI of energetic materials, photofragmentation of the EM produces NO, as just described in section 5.3. The maximum NO$^+$ yield from REMPI occurs at 226.3 nm, corresponding to a (1+1) process via the A $^2\Sigma(v=0)\leftarrow X^2\Pi_{1/2}(v=0)$ transition (*165*).

In 1990, Zhu et al. performed resonant two-photon ionization (R2PI) at 266 and 213 nm of substituted nitrobenzenes (*152*). Typically in REMPI, the molecular ion itself is not observed for large parent molecules. They found that although extensive fragmentation occurs under vacuum, R2PI under atmospheric pressure (1 atm, He) has the potential of being a soft ionization source for even very fragile molecules. From their study of *p*-nitroaniline, *o*-nitroaniline, nitroanisole, nitrophenol, nitrotoluene, 2,6-DNT, 2,4-DNT, and 2,4,6-TNT, they showed that unique ions are produced for the different isomers.

Clark et al. developed a very sensitive and selective procedure for the detection of nitroaromatic vapors (*141*). Not only were they able to distinguish NB and *o*-nitrotoluene, two of the simplest explosive compounds, they could also distinguish NO$^+$ from NO/NO$_2$ gases and nitroaromatic compounds by their laser-induced mass spectra and wavelength dependence (245–250 nm) of the fragment ions. In addition, they demonstrated subattomole (<10^{-18} M) sensitivity for nitrobenzene via generation of intense NO$^+$ ion signals using REMPI at 226.3 nm.
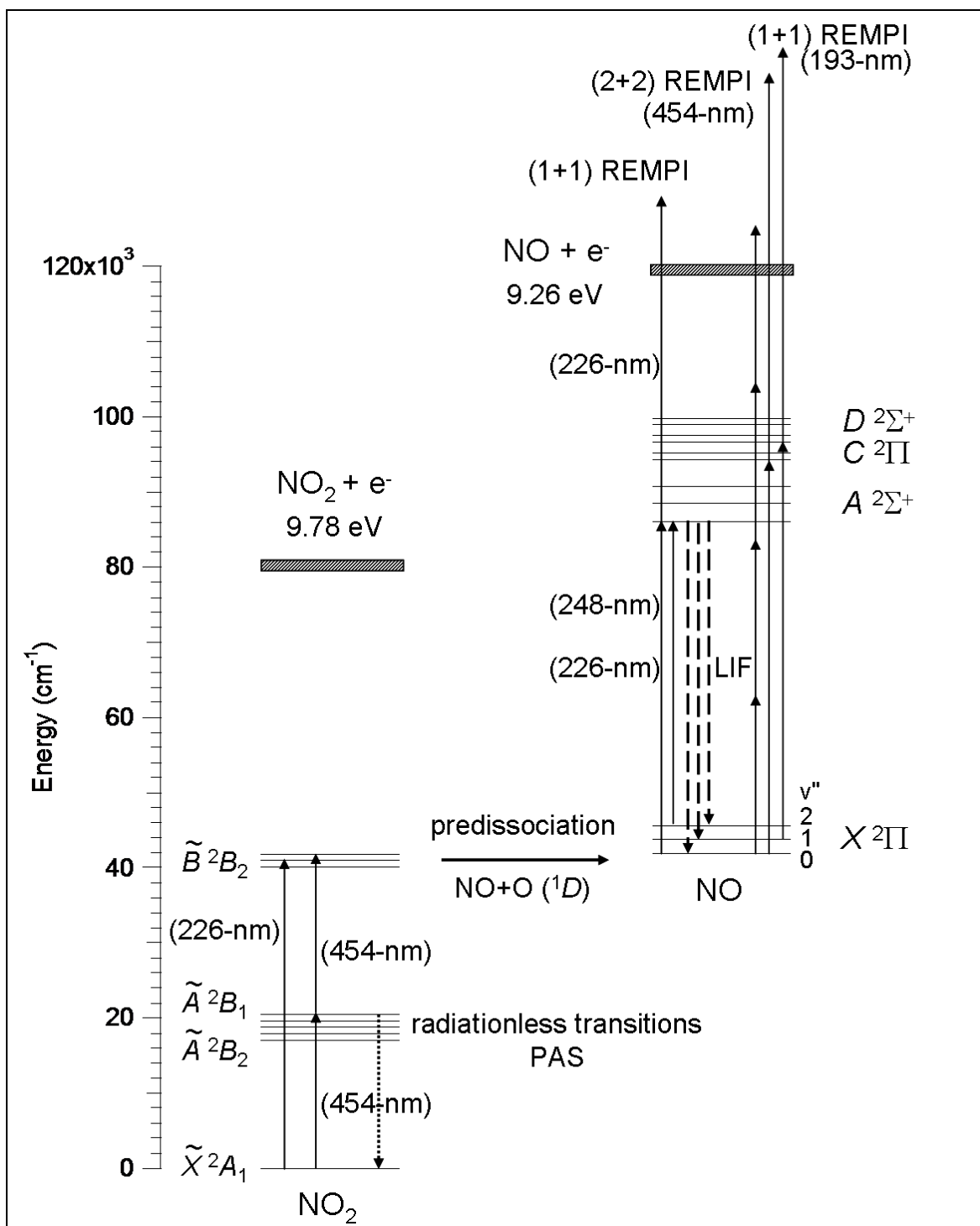
Figure 17. Partial energy level diagram of NO_2 and NO. Several detection schemes including REMPI, LIF, and PAS are shown using laser wavelengths of 193, 226, and 454 nm.

On the basis of the high degree of sensitivity and selectivity for NO fragments that can be achieved by (1+1) REMPI, Lemire et al. developed a novel technique for sensing trace vapors of NO_2-containing compounds (*142*). They pointed out that one laser tuned to 226 nm can be used for photofragmentation and then excitation of the resulting NO fragments. Samples studied with this method included NB, TNT, and RDX, with detection limits of 2.4 ppm, 24 ppb, and 8 ppb, respectively, using REMPI and time-of-flight mass spectrometry (TOF-MS). One drawback to this method was that it utilized a complex, excimer-pumped dye laser system with second harmonic generation.

Simeonsson et al. used an ArF laser to photolytically fragment the target molecules and ionize the characteristic NO fragments (*143*). Ionization of the NO molecules was through REMPI processes via its $A\,^2\Sigma^+ \leftarrow X\,^2\Pi(3,0)$, $B\,^2\Pi \leftarrow X\,^2\Pi(7,0)$, and/or $D\,^2\Sigma^+ \leftarrow X\,^2\Pi(0,1)$ bands at 193 nm. Limits of detection at 193 nm for NB, NT, and TNT were 0.49 ppm, 0.10–0.12 ppm, and 0.21 ppm, respectively, compared to 2.4 ppm, 15–36 ppm, and 1.7 ppm at 226 nm. The photofragmentation/ionization TOF mass spectra were used to discriminate between the structural isomers of NT (*ortho-* and *meta*-nitrotoluene). In a subsequent paper, the authors used a simplified experimental apparatus with a pair of miniature electrodes for ion detection (*175*). Although they detected NO with (1+1) REMPI by means of its $A\,^2\Sigma^+ \leftarrow X\,^2\Pi(0,0)$ transitions near 226-nm (LOD 1 ppb) and NO_2 by laser photofragmentation with subsequent NO fragment ionization (LOD 22 ppb), the two species could not be differentiated.

The photodissociation of NO_2 into NO+O is energetically permitted at wavelengths less than 400 nm, with the maximum of the absorption process between 380–400 nm. Since three or four photons (at 266 nm) or four photons (at 380 nm) are required for photodissociation and ionization, the sensitivity in air is not as high as for NO. The detection limit for NO_2 in air is about 10 ppb at a laser wavelength of 380 nm (*165*). NO has a characteristic double headed, two photon ionization spectrum at 226.4 nm and 227 nm, but nearby features in the spectrum belonging to multiphoton ionization processes in molecular oxygen reduce the sensitivity (*165*). Guizard et al. (*176*) suggested a (2+1) ionization scheme via the $C\,^2\Pi(v{=}0) \leftarrow X\,^2\Pi(v{=}0)$ transition at 380 nm, which avoids the problems associated with the molecular peaks of oxygen. Ledingham (*165*) later demonstrated an LOD for NO of about 100 ppt using this scheme.

Simeonsson and Sausa (*167*) detected NO near 452 nm by (2+2) REMPI via its $A\,^2\Sigma^+ \text{-} X\,^2\Pi(0,0)$ and (1,1) transitions, while NO_2 was detected by laser photofragmentation to NO followed by ionization. Detection was performed using a pair of miniature electrodes. They found that spectral differentiation was possible because the internal energy of the NO photofragments differed from the "ambient" NO. Measurement of the vibrationally excited NO via its $A\,^2\Sigma^+ \text{-} X\,^2\Pi(0,3)$ band at 517 nm was also demonstrated. The limits of detection for NO and NO_2 were under 100 ppb (20–40 ppb_v at 449–452 nm and 75 ppb_v at 517.5 nm). Discrimination between NO and NO_2 photofragment detection at 226 nm was also demonstrated (*177*). A 2001 ARL technical report summarized the extensive work done using PF-REMPI (and PF-LIF) of explosives at ARL by Sausa and coworkers (*178*).

Schmidt et al. developed an atmospheric pressure laser ionization source based on REMPI in pulsed gas expansions close to the inlet nozzle orifice (at high molecule densities) of their mass spectrometer (*174*). Their approach was to shift the ionization volume to the high-pressure continuous flow regime of expansion, where high particle densities predominate in order to significantly enhance the REMPI detection limit in mass spectrometric applications (with TOF-MS). The sampling stage allowed for measurements of reactive or thermally unstable species. This arrangement gave a LOD for NO of 0.9 ppt, an improvement of a factor of roughly 400 over a conventional skimmed molecular beam setup.

5.2.1.2 PF-LIF

A second technique frequently used to detect photofragmented species is LIF. Unlike UV/Vis or other absorbance spectroscopy, fluorescence is a zero-background method and provides high sensitivity and selectivity when a laser is used as the excitation source. In this technique, the laser is tuned so that its frequency matches that of an absorption line of some atom or molecule of interest. The absorption of the photons by this species produces an electronically excited state, which then radiates producing fluorescence emission characteristic of the species. Rodgers et al. were the first to suggest a new method for the in situ detection of nonfluorescing molecular species by combining PF and LIF (PF-LIF) (*179*). The species is first photolyzed at wavelength λ_1, producing one or more vibrationally excited fragments. Prior to vibrational relaxation, the resulting photofragments are pumped into a bonding excited state by a second laser pulse at wavelength λ_2. The fluorescence is sampled at wavelength λ_3, where $\lambda_3 < \lambda_2$ and λ_1. They demonstrated this technique on NO_2 (among other atmospheric gases) and estimated a detection limit of 3 ppt.

Zuckermann et al. studied IRMPD of RDX and HMX in a supersonic jet (*147*). A CO_2 laser was used for dissociation, with a pulsed frequency-doubled dye laser tuned to 280-nm to excite the A $^2\Sigma(v=1)\leftarrow X\,^2\Pi(v=0)$ transition of OH. OH radicals were observed by LIF, indicating that OH loss is a primary process in the unimolecular dissociation of nitramines such as RDX and HDX. Guo et al. employed UV excitation to study the decomposition of RDX and HMX from their first excited electronic states (*180*). NO was observed as one of the initial dissociation products using both TOF-MS and LIF. Because the LIF of OH is well known and quite intense, they decided to look for it as well. Despite a calculated transition intensity 1.5× that of NO, however, the OH radical was not observed as a UV dissociation product using LIF.

Wu et al. developed a technique based on photofragmentation followed by LIF of NO (PF-LIF) to measure the concentration of energetic materials in soil and other media (*156*). Laser radiation near 226 nm was used to photodissociate the EM to NO_2, which predissociated into NO. The ground state NO then absorbed a second 226-nm photon to undergo a resonant transition $A\,^2\Sigma^+$ ($v'=0)\leftarrow X\,^2\Pi$ ($v''=0$), subsequently producing NO $A\,^2\Sigma^+$ ($v'=0)\rightarrow X\,^2\Pi$ ($v''=n$) fluorescence. The concentration of the EM was inferred from the intensity of the NO fluorescence. They found that the PF-LIF signal intensity significantly increases when the

sample (TNT) was heated in an oven above 343 K, but that heating causes physical and chemical changes in the sample. The LOD of TNT in soil was estimated to be 40 ppb. Factors influencing the PF-LIF signal, such as sample temperature, laser power, and heating time, were investigated in a subsequent paper (*157*). The LOD for 2-μJ laser power and a TNT sample temperature of 473 K was 4 ppm. The suitability of the technique for field implementation was discussed, along with plans to develop a PF-LIF laser-based sensor for use with the U.S. Army Corps of Engineers' Waterways Experiment Station's cone penetrometer in order to measure the concentration of subsurface TNT in situ.

In 1999, Swayambunathan et al. detected trace concentrations of TNT, PETN, and RDX by laser PF-FD spectrometry using both PF-REMPI (with miniature electrodes) and PF-LIF in air with limits of detection in the low ppb-ppm range (*148*). They determined that collisional quenching of NO ($A\,^2\Sigma^+$) by N_2 and O_2 and reactions with O_2 were more pronounced in the LIF experiments than in the REMPI experiments because the radiative lifetime of the $A\,^2\Sigma^+$ intermediate state is relatively long, ~215 ns. In contrast, ionization from the intermediate $A\,^2\Sigma^+$ state was instantaneous (within the 6-ns laser pulse) in REMPI, allowing little time for quenching and other reactions to occur. In addition, nearly all the ions produced by REMPI were collected by the electrodes, while only part of the signal in the LIF experiments was collected (the fluorescence was viewed through a small cone in a direction perpendicular to the excitation beam). Consequently, the LIF signals for RDX and PETN were very weak for room-temperature samples. However, the LIF intensity increased with increasing temperatures above the melting point (~413 K for PETN and 476–477 K for RDX). The pyrolysis-LIF technique involved pyrolysis of the energetic material in an oven with subsequent detection of the pyrolysis products NO and NO_2 by LIF (227 nm) and PF-LIF (454 nm), respectively (*178*). PF-FD experiments on EMs were also performed with a visible laser because of the potential advantages compared to an ultraviolet laser—namely, that the laser can be easily transmitted through optical fibers over 10–30-m distances. Their studies showed that using 454 nm resulted in a lower photofragmentation efficiency and a higher LOD for PF-REMPI. Using 454 nm also resulted in lower NO excitation efficiency for pyrolysis-LIF and therefore a higher LOD.

Daugey et al. demonstrated one-color (the same wavelength is used for photofragmentation and excitation of the fragments) PF-LIF detection of NB using 222–272 nm photodissociation and detection of NO via the A (v'=0)-X (v''=0–4) transitions (*144*). They found that in addition to the vibrationless ground state NO, a significant amount of vibrationally excited NO was also produced and can be detected free from interference by atmospheric NO. An LOD ~500 ppb in air (10 and 100 Torr) was achieved by monitoring NO through excitation of the $A\,^2\Sigma^+$ (v'=0)← X $^2\Pi$ (v''=2) transition and detection via $A\,^2\Sigma^+$ (v'=0)→ $X\,^2\Pi$ (v''=1) at ~236 nm. Shu et al. then detected trace concentrations of DNB with an LOD of 13 ppb in 100 Torr of air and 11 ppb in 500 Torr of air using 248-nm dissociation and excitation (*146*). As with the previous study on NB, the fluorescence was collected at shorter wavelengths than the exciting radiation, precluding background fluorescence or ambient ground-state NO interference. This technique was

subsequently used to detect DNT with an LOD of 3.7 ppb in 100 Torr of air and 2.7 ppb in 500 Torr of air (*154*, *181*).

Arusi-Parpar et al. developed a unique scheme to remotely detect trace amounts of TNT vapor at atmospheric pressure and 24 °C using a single 248-nm laser beam (*158*). Detection was based on the photodissociation of TNT vapor followed by LIF of the $A\,^2\Sigma^+$ (v'=0) $\leftarrow X\,^2\Pi$ (v''=2) transition of the NO photofragments (LOD <8 ppb). The authors estimated that at least 30% of the photodissociated TNT molecules produced NO with a v''=0, 1, 2 ratio of 1:0.5:0.1. As demonstrated by Shu et al. (*144*, *146*, *154*, *181*) at low pressures, there were two important advantages in detecting vibrationally excited NO radicals vs. the ground-state NO produced by photodissociation: (1) the collected fluorescence was at lower wavelengths than the exciting laser (in contrast with the fluorescence from either the TNT molecule or other molecules that exist in air), and (2) there was no fluorescence from the ground-state NO that is present naturally in air (which reduces the probability of a false alarm). Ambient conditions dramatically shortened the NO fluorescence lifetime, mainly due to quenching by oxygen. Using relatively high laser energy (~5 mJ), a large interaction volume (unfocused laser), an improved detection system (with tailor-made spectral filters), and a background-free scheme, they were able to develop a more sensitive detection system than Wu et al. (*156*) or Swayambunathan et al. (*148*). This technique was later demonstrated at 2.5 m under near-ambient conditions (1 atm and 28 °C), with an LOD < 15 ppb (*159*).

5.2.2 Femtosecond Ionization/Dissociation

Photounstable molecules such as nitro-compounds tend to quickly dissociate after photoexcitation by a nanosecond laser, which greatly reduces the probability for the absorption of the additional photons necessary for ionization. The resulting photofragments are not specific enough to unambiguously identify the parent molecule. Ultrashort-pulse laser radiation provides high intensities (10^{12} to 10^{17} W cm^{-2}) and pulse durations shorter than the rotational timescales of molecules. It has been demonstrated that using ultrashort pulses decreases the interaction time such that the multiphoton ionization process is finished before the intermediate energy level can be depleted through fast relaxation processes (e.g., intramolecular energy redistribution due to internal conversion, intersystem crossing, or fast dissociation processes). A review by Ledingham and Singhal (*182*) discussed the use of ultrafast lasers for photofragmentation /ionization.

Kosmidis et al. compared 90-fs photodissociation of NB and NT isomers at 375 nm to 10-ns photodissociation at the same wavelength (*183*). They demonstrated that only the femtosecond laser produced parent and heavy mass peaks (figure 18). A nonresonant multiphoton process resulted in molecular ionization. The mass spectra of the three NT isomers had analytically differentiable spectra. Using multiphoton excitation of nitrotoluene compounds with 170-fs laser pulses at either 412 nm or 206 nm, Tonnies et al. demonstrated that the mass spectra of NT,
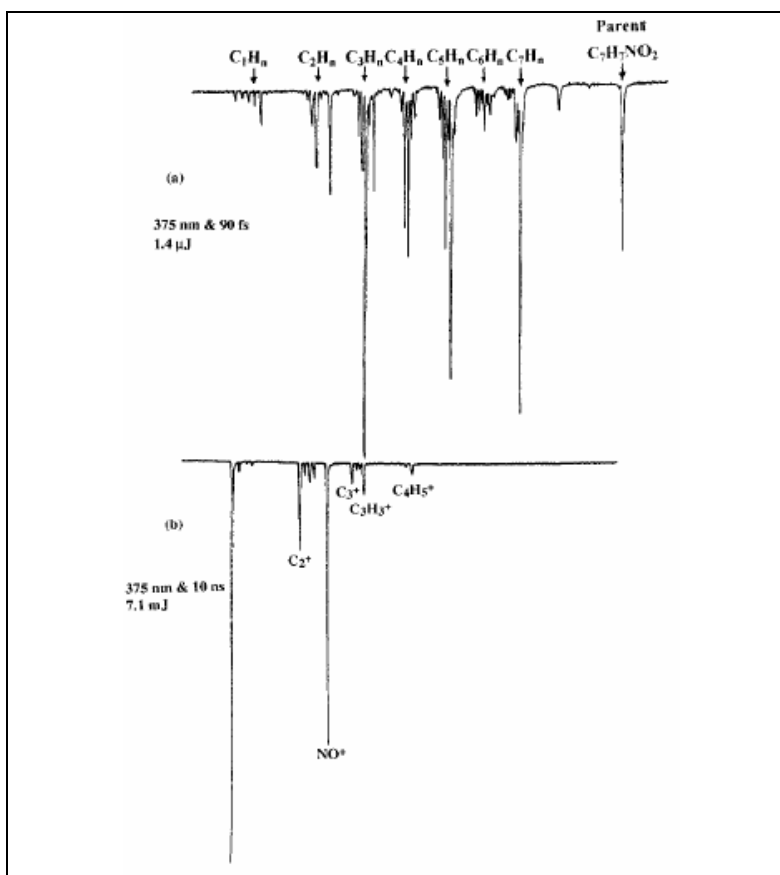
Note: Reprinted with permission from Kosmidis et al. (*183*); copyright (1997)
American Chemical Society.

Figure 18. Comparison of femtosecond and nanosecond fragmentation
spectra of *m*-nitrotoluene at 375-nm. Only the 90-fs laser
pulse shows parent and heavy mass peaks, while the 10-ns
laser pulse results in much smaller photofragments.

DNT, and TNT exhibit a clear molecular ion or OH signal despite intense fragmentation (*184*).
The two-photon absorption at 206 nm and four-photon absorption at 412 nm was not resonantly
enhanced. They found that the intensity of the molecular ion signal decreased with increasing
substitution and that mass spectra obtained at 412 nm showed a higher degree of fragmentation
than those at 206 nm. Isomer-specific detection after multiphoton ionization was demonstrated
at both wavelengths for two isomers of NT and only at 412 nm for two of the DNT isomers. In a
continuation of the work of Tonnies et al. (*184*), Weickhardt and Tonnies obtained mass spectra
of all isomers of NT and four isomers of DNT using ultrashort laser pulses at 206 nm or 412 nm
(*185*). Compounds with a nitro-group in position 2 and/or 6 showed a pronounced ortho effect
leading to the loss of OH. The 412-nm light resulted in a broader variety of fragments and
additional signals in the higher mass range that could be used for isomer identification.

Hankin et al. demonstrated femtosecond ionization following 266-nm desorption of solid samples of trinitrobenzene, TNT, and trinitrophenol (*186*). They confirmed the advantages of ultrafast ionization, namely the formation of characteristic precursor and structure-specific fragment ions. The optimum intensities for efficient laser desorption without ionization were determined for the compounds studied. Differences between femtosecond ionization of vapor samples of explosives (*184*, *185*) and laser desorbed molecules were also discussed.

Osorio et al. performed TOF-MS measurements of TNT and RDX on soil surfaces (*187*). They used tunable UV radiation from a 130-fs laser to monitor the kinetic energy distribution of NO/NO_2 photofragments released by the dissociation of TNT and RDX. Analysis of the kinetic energy distribution of the photofragments revealed differences in the processes for NO and NO_2 ejection in different substrates. Mullen et al. detected TATP by laser photoionization (*161*). Mass spectra in two time regimes were acquired using nanosecond (5 ns) laser pulses at 266 and 355 nm and femtosecond (130 fs) laser pulses at 795, 500, and 325 nm. The major difference observed between the two time regimes was the detection of the parent molecular ion when femtosecond laser pulses were employed.

5.2.3 Surface Photofragmentation-Fragment Detection (SPF-FD)

Cabalo and Sausa introduced a technique for detection of explosives with low vapor pressure called SPF-FD (*149*). Although techniques such as CRDS, PF-LIF, and PF-REMPI are ideal for TNT in the gas phase, the vapor pressure of most explosives is too low to detect using those methods, especially at room temperature. In SPF-FD, a UV laser (248, 266, or 355 nm) is used to photofragment RDX on a surface, and a second time-delayed laser (226 nm) ionizes the characteristic NO fragment by means of its $A\,^2\Sigma^+$-$X\,^2\Pi$ (0,0) transitions by (1+1) REMPI (SPF-REMPI). The maximum signal was observed with a photolysis wavelength of 248 nm, where the absorption coefficient of RDX is the strongest. A detection limit of ~14 ng/cm^2 at 1 atm and 298 K was demonstrated.

5.2.4 SPI-TOF-MS

Mullen et al. demonstrated the detection of energetic materials using single photon laser ionization (SPI) (*145*). Although ultrafast ionization has been successfully applied to the selective detection of explosives, the complex, nonruggedized instrumentation required makes the technique unsuitable for field scenarios. SPI is a more robust ionization method that does not involve resonant excitation of an intermediate state (unlike REMPI)—the parent molecule is directly ionized using a vacuum ultraviolet (VUV) photon. By frequency tripling the third harmonic output (354.6 nm) of a Nd:YAG laser in xenon, 118.2-nm (10.49-eV) photons can be generated. At these energies, atmospheric gases such as nitrogen, oxygen, and water vapor do not have sufficient energy to ionize directly; however, most organic compounds do ionize. Ions of energetic materials produced by two or more VUV photons are detected using TOF-MS (SPI-TOF-MS). Vapors from the samples (NB, 1,3-DNB, *o*-NT, 2,4-DNT, 2,4,6-TNT, and TATP)

were introduced into the instrument using a capillary gas chromatography (GC) column. They found that SPI of the nitro-containing explosives yields mass spectra dominated by the parent molecular ion, although TATP undergoes extensive fragmentation. Limits of detection were determined for NB (17–24 ppb) and DNT (~40 ppb).

5.3   PAS

PAS is an indirect detection method that measures thermal energy imparted to a gas (usually monatomic) in close contact with a photoexcited material (solid, liquid, or gas). Following sample photoexcitation, energy is rapidly transferred to the surrounding gas. If the photoexcitation is modulated at an acoustic frequency, the resulting thermal pulse in the surrounding gas may be detected by a microphone (*188*). High-resolution photoacoustic spectra are measured using either a pulsed laser or a wavelength- or amplitude-modulated (e.g., with a mechanical chopper) light source. PAS is an attractive technique because of its relative simplicity, ruggedness, and overall sensitivity. In addition to obtaining absorption spectra, PAS can be used to measure collisional relaxation rates, determine substance compositions, and monitor reactions (*189*).

Because optoacoustic detectors respond only to absorbed radiation, much weaker absorptions can be detected than with traditional absorption spectroscopy methods, which depend on detecting small differences between large signals (*190*). It is particularly effective at high pressures for weak fluorescing species or species that predissociate with laser absorption (*173*). The magnitude of the measured photoacoustic signal is given by $S=S_mPC\alpha$, where C is a cell-specific constant (units of Pascal centimeters per watt), P is the power of the incident laser radiation (watts), α is the absorption coefficient of the transition that is being interrogated (cm^{-1}), and S_m is the sensitivity of the microphone (volts per Pascal) (*191*). Because the signal is proportional to the incident laser power, the detection sensitivity of trace gases improves with the use of higher laser powers. This technique is also well suited to diode laser spectroscopy of explosives, where the laser bandwidth is much narrower than the absorber bandwidth (see section 2.1.1).

In 1972, Kreuzer et al. (*192*) demonstrated the optoacoustic detection of 10 pollutant gases using CO and CO_2 lasers, including 0.1-ppb detection of NO_2 at 6.22 μm. Claspy and coworkers (*150*) were the first to detect explosive vapors using PAS. Periodic heating with a chopped IR beam (5.8–6.7 μm) of a cell containing the vapor sample resulted in pressure fluctuations that were detected with a sensitive microphone. They identified EGDN, DNT, TNT, dynamite, RDX, and PETN in the atmosphere at partial pressures of 10^{-6} Torr or less (on the order of ppb) with their system. In 1975, Angus et al. reported the first use of a tunable visible laser with an optoacoustic cell (*190*), estimating a 10-ppb NO_2 detection limit from low-resolution continuous wave (CW) dye laser excitation scans over the 575–625-nm range. Subsequent studies by Claspy and colleagues investigated atmospheric interferents (NO, NO_2, CH_4, C_4H_{10}, and H_2O) for explosives detection at 6, 9, and 11 μm (*139*) and used a pulsed dye laser (480–625 nm) to detect NO_2 with 4-ppb sensitivity at 600 nm (*193*).

Terhune and Anderson (*194*) measured NO_2 sensitivities of better than 0.1 ppb during in situ measurements of aerosols using an acoustically resonant spectrophone and a 514.5-nm Ar^+-ion laser. By constructing a nonmetal cell to minimize surface adsorption, Crane (*140*) was able to use a CO_2 laser (9.6 μm) to obtain optoacoustic absorption spectra of EGDN, DNT, and NG vapors with LOD of 8.26-, 0.23-, and 0.50-ppb, respectively. Water vapor, which occurs in high concentrations in air and absorbs throughout the IR, was found to be the limiting interferent. Fried (*195*) measured the 488-nm PAS detection limit of NO_2 in NO, N_2, H_2O, and O_2 matrices with identical sensitivities of 5 ppb in all matrices except O_2, which decreased the NO_2 signal. A possible explanation given is that the energy deposited into the NO_2 molecules was transferred to O_2 instead of being released as heat, thus degrading the optoacoustic signal.

In 1995, Hasue et al. (*188*) reported low-resolution photoacoustic spectra of 18 powdered energetic materials. A 500-W xenon lamp was used as a light source for coverage from 400 to 800 nm, and a 300-W halogen lamp for 800–1600 nm. In general, energetic materials showed peaks in the 600–800-nm and 1400–1600-nm ranges. Spectra of picric acid, TNT, PETN, ammonium perchlorate, tetryl, composition-B, dinitromethyloxamide, RDX, HMX, black powder, potassium nitrate, ammonium nitrate fuel oil, composition C-4, composition A-3, Hexal, nitroguanidine, and N,N'-dinitro-1,2-ethanediamine were obtained. The energy required to initiate explosives with a ruby laser at 694.3 nm was also correlated with their photoacoustic signals at that wavelength. The acquired spectra for Hexal and PETN demonstrated that aluminum and active carbon improve the absorption of laser light for EMs at 820 nm.

Pastel and Sausa (*173*) detected NO_2 (LOD 400 ppb at 1 atm) with a one-photon absorption photoacoustic process (see figure 17) by means of $\tilde{A}'\,^2B_1(0,8,0)$-$\tilde{X}\,^2A_1(0,0,0)$. This work, which employed a dye laser operating near 454 nm, was the first report of a high-resolution visible NO_2 photoacoustic spectrum. They found that low laser intensities favored NO_2 photoacoustic detection, whereas high laser intensities favored NO detection via REMPI (LOD 160 ppb). Figure 19 shows the high-resolution photoacoustic spectrum of NO_2 and the NO REMPI spectrum.

Prasad et al. (*151*) used vibrational PAS in conjunction with published conventional IR data and ab initio calculations to assign the normal modes of RDX and TNT. The IR PAS measurements on powder samples were made using a line-tunable CW CO_2 laser source. They found that the most suitable bands of TNT for spectrochemical analysis were at 978 cm^{-1} (C-H out of plane bending) and 946 cm^{-1} (C-N stretching motions); for RDX, the persistent bands were at 1045 cm^{-1} (N-N stretching) and 941 cm^{-1} (O-N-O bending motions).

More than 30 years of research have shown that explosive vapor detection using PAS is limited by surface adsorption and decomposition at elevated temperatures. The technique is also limited by interferents, especially in the IR (e.g., water vapor in air). However, several promising new methods for PAS have recently been suggested. Webber et al. (*191*) incorporated near-IR diode lasers and optical fiber amplifiers to enhance sensitivity. This new approach to wavelength
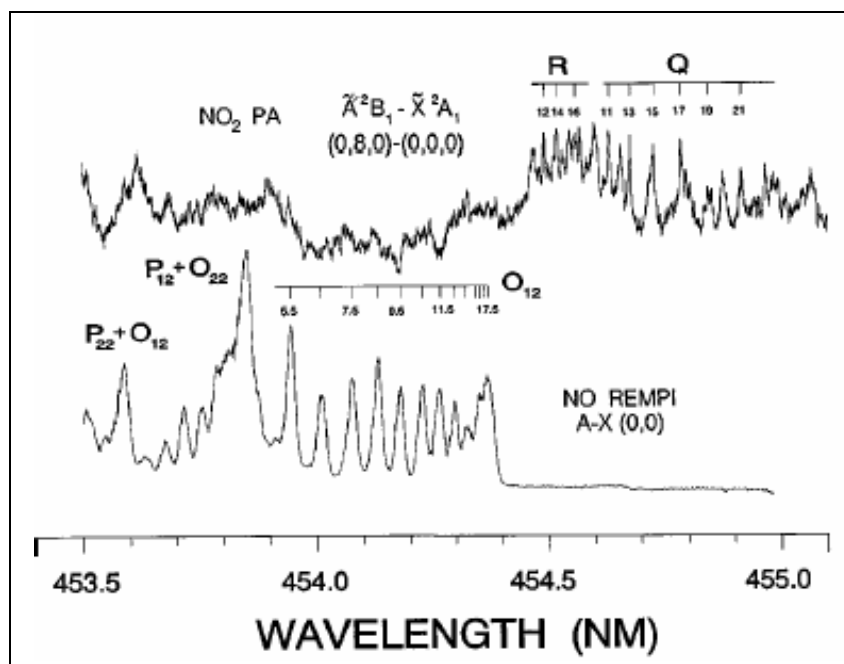
Note: Reproduced with permission from Pastel and Sausa (*173*).

Figure 19. High-resolution photoacoustic spectrum of NO_2 (top) and REMPI
spectrum of NO (bottom).

modulation photoacoustic spectroscopy is applicable to all species that fall within the gain curves
of optical fiber amplifiers. By wavelength-modulating the laser, the acoustic signals from
wavelength-independent sources such as window absorption and continuum spectra from
broadband absorbers are eliminated by demodulation. They demonstrated the technique, which
first used fiber amplifiers to enhance PAS, with ammonia detection at 1532 nm (LOD <6 ppb).
The same group recently evaluated the performance of a field deployable tunable CO_2 laser
photoacoustic spectrometer, demonstrating detection of chemical warfare agents at 4 ppb with a
probability of false positives less than $1:10^6$. Because CO_2 lasers could not provide continuous
tuning, they also discussed the use of QC lasers for PAS.

5.4   LIDAR Variations

Several systems based on LIDAR (see section 2.3) have been developed for explosives and
explosive device detection. While not fitting the conventional LIDAR experiment definition,
these systems apply LIDAR principles to the detection of explosive sources.

Simonson et al. (*160*) demonstrated remote detection of explosives in soil by combining
distributed sensor particles with UV/Vis fluorescence LIDAR technology. The key to this
approach is that the fluorescence emission spectrum of the distributed particles is strongly
affected by absorption of nitroaromatic explosives from the surrounding environment. Remote
sensing of the fluorescence quenching by TNT or DNT is achieved by fluorescence LIDAR. The
emission spectra were excited in field LIDAR measurements by a frequency-tripled Nd:YAG

laser at 355 nm, and the fluorescence collected with a telescope and various detector systems housed in a 10- × 50-ft trailer. TNT has been detected in the ppm range at a standoff distance of 0.5 km with this system (see figure 20). An important limitation to this technique is the preconcentration of the explosives on the sensor particles, which requires the presence of water to facilitate the transport of the explosive from the surface of the soil particles to the sensor particles.
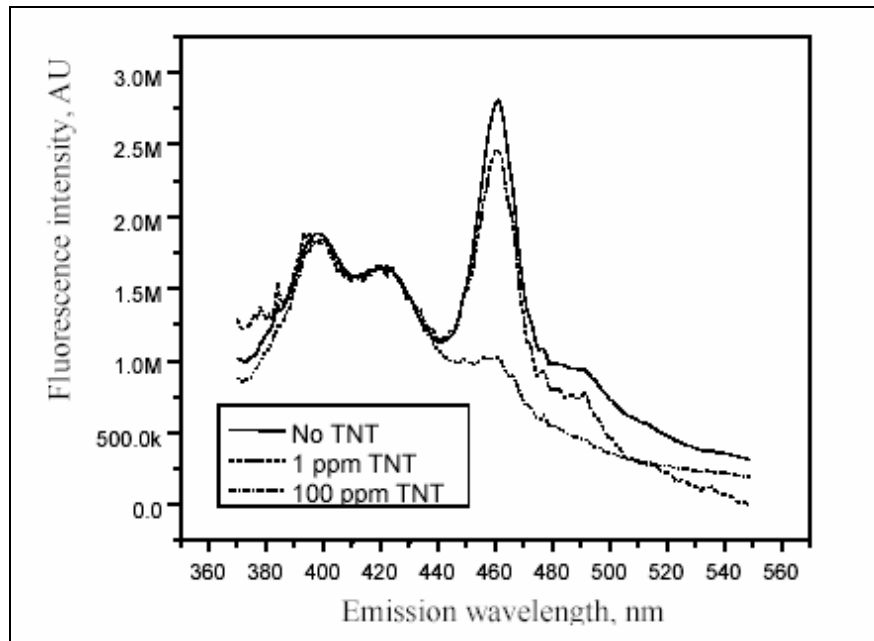
Note: Reproduced with permission from Simonson et al. (*160*).

Figure 20. Laboratory-collected fluorescence emission from sensor particles on soil contaminated with TNT.

Xiang and Sabatier (*196*) used a scanning laser Doppler vibrometer (LDV) to detect acoustic-to-seismic surface motion. This technique exploits airborne acoustic waves penetrating the ground and causing seismic motion. When an antipersonnel landmine is buried in the soil, the acoustically coupled ground motion is altered. The LDV measures the motion of the ground surface since the surface vibration causes a Doppler frequency shift of the reflected laser light. Color maps can be formed which image the mine location, size, and shape. Although mines can be identified with a high probability of detection with this technique, ground clutter can cause high false alarm rates.

Finally, LIDAR has been used to detect honeybees trained to search for leached explosives (*197–199*). Honeybees are faster to train than dogs, do not need to be leashed, and will not set off landmines. They can also detect explosives with sensitivity comparable to, or better than dogs (low ppt or ppq) at a 1–2-km range. When the honeybees detect the explosive, they hover over the sample location before returning to the hive. Direct LIDAR has been used to map the areas of highest bee concentration, but a clear line of sight with no vegetation or other obstructions

is needed (*199*). Recently, it was demonstrated that a frequency-modulated signal resulting from the light scattered off honeybee wings (170–270 Hz) could be used to discriminate the return signal of a honeybee from the cluttered background (*200*).

5.5 Photoluminescence

Photoluminescence is a process in which a molecule absorbs a photon in the visible region, exciting one of its electrons to a higher electronic excited state, and then radiates a photon as the electron returns to a lower energy state. If the molecule undergoes internal energy redistribution after the initial photon absorption, the radiated photon has a longer wavelength (i.e., lower energy) than the absorbed photon. Fluorescence and phosphorescence (when intersystem crossing results in a transition of the electron to a state of higher spin multiplicity) are special forms of photoluminescence.

Germanenko et al. (*200*) suggested an explosives detector based on the quenching of silicon photoluminescence by nitrotoluenes. Silicon nanocrystals are first prepared by laser vaporization. After suspension in methanol, the Si nanocrstyals are excited by a laser at 355 nm, resulting in photoluminescence. They found that aromatic nitro-compounds quench the photoluminescence from the Si nanocrystals. Quenching rate constants for 3,5-dinitrobenzonitrile, 4-nitrophthalonitrile, 1,4-dinitrobenzene, 4-nitrobenzonitrile, 2,3-dinitrotoluene, 3,4-dinitrotoluene, 2,4-dinitrotoluene, and 2,6-dinitrotoluene were found to be in the range of $10^{-6} - 10^{-7}\,M^{-1}s^{-1}$.

6. References

1. Steinfeld, J. I.; Wormhoudt, J. *Annu. Rev. Phys. Chem.* **1998**, *49*, 203.

2. Henderson, D. O.; Tung, Y. S.; Mu, R.; Ueda, A.; Curby, W.; Mercado, A. G.; Li, X. *Trends Appl. Spectrosc.* **1998**, *2*, 139.

3. Moore, D. S. *Rev. Sci. Instrum.*, **2004**, *75*, 2499.

4. Dionne, B. C.; Rounbehler, D. P.; Achter, E. K.; Hobbs, J. R.; Fine, D. H. *J. Energ. Mat.* **1986**, *4*, 447.

5. Pella, P. A. *J. Chem. Thermodyn.* **1977**, *9*, 301.

6. Jenkins, T. F.; Leggett, D. C.; Ranney, T. A. *Vapor Signatures from Military Explosives Part 1. Vapor Transport from Buried Military-Grade Tnt*; Special Report 99–21; Office of the Chief Engineers, U.S. Army Corps of Engineers: Cold Regions Research and Engineering Laboratory, Hanover, NH, 1999.

7. Beal, R. W.; Brill, T. B. *Appl. Spectrosc.* **2005**, *59*, 1194.

8. Sedlacek, A. J., III; Christesen, S. D.; Chyba, T.; Ponsardin, P. *Proc SPIE-Int. Soc. Opt. Eng.*, **2004**, *23*, 5269.

9. Herzberg, G. *Vol I. Spectra of Diatomic Molecules, and Vol II. Infrared and Raman Spectra*; New York: Van Nostrand Rheinhold, 1945.

10. McNesby, K. L.; Pesce-Rodriguez, R. A. *Applications of Vibrational Spectroscopy in the Study of Explosives in Handbook of Vibrational Spectroscopy*; Chalmers, J. M., Griffiths, P. R., Eds.; John Wiley and Sons: West Sussex, UK, 2002; p 3152.

11. Fell, N. F.; Widder, J. W.; Medlin, S. V.; Morris, J. B.; Pesce-Rodriguez, R. A.; McNesby, K. L. *J. Raman Spectrosc.* **1996**, *27*, 97.

12. Silver, J. A. *Appl. Opt.* **1992**, *31*, 707.

13. Schultz, J. F.; Taubman, M. S.; Harper, W. W.; Williams, R. M.; Myers, T. L.; Cannon, B. D.; Sheen, D. M.; Anheier, N. C., Jr.; Allen, P. J.; Sundaram, S. K.; Johnson, B. R.; Acker, P. M.; Wu, M. C.; Lau, E. K. *Proc. SPIE-Int. Soc. Opt. Eng.* **2003**, *1*, 4999.

14. Allen, M. G.; Cook, D. J.; Decker, B. K.; Hensley, J. M.; Rosen, D. I.; Silva, M. L.; Sonnenfroh, D. M.; Wainner, R. T. *Proc. SPIE-Int. Soc. Opt. Eng.* **2005**, *134*, 5732.

15. Wormhoudt, J.; Shorter, J. H.; Kolb, C. E. *Mater. Res. Soc. Symp. Proc.* **1996**, *418*, 143.

16. Riris, H.; Carlisle, C. B.; McMillen, D. F.; Cooper, D. E. *Appl. Opt.* **1996**, *35*, 4694.

17. Bauer, C.; Geiser, P.; Burgmeier, J.; Holl, G.; Schade, W. *Appl. Phys. B* **2006**, *85*, 251.

18. Effenberger, F. J.; Mercado, A. G. *Proc. SPIE-Int. Soc. Opt. Eng.* **1998**, *104*, 3384.

19. Todd, M. W.; Provencal, R. A.; Owano, T. G.; Paldus, B. A.; Kachanov, A.; Vodopyanov, K. L.; Hunter, M.; Coy, S. L.; Steinfeld, J. I.; Arnold, J. T. *Appl. Phys. B* **2002**, *75*, 367.

20. Vaicikauskas, V.; Kabelka, V.; Kuprionis, Z.; Kaucikas, M. *Proc. SPIE-Int. Soc. Opt. Eng.* **2005**, *5958*, 59581K:1.

21. Chaudhary, A. K.; Bhar, G. C.; Das, S. *J. Appl. Spectrosc.* **2006**, *73*, 123.

22. McKnight, S. W.; DiMarzio, C. A.; Li, W.; Roy, R. A. *Proc. SPIE-Int. Soc. Opt. Eng.* **2000**, *4038*, 734.

23. Kim, H.; Lagutchev, A.; Dlott, D. D. *Propell. Explos. Pyrot.* **2006**, *31*, 116.

24. Busch, W. W.; Busch, M. A., Eds. *An Ultratrace-Absorption Measurement, Acs Symposium Series*; Vol. 720, American Chemical Society: Washington, DC, 1999.

25. Spicer, J. B.; Dagdigian, P. J.; Osiander, R.; Miragliotta, J. A.; Zhang, X.-C.; Kersting, R.; Crosley, D. R.; Hanson, R. K.; Jeffries, J. *Proc. SPIE-Int. Soc. Opt. Eng.* **2003**, *5089*, 1088.

26. Steinfeld, J. I.; Field, R. W.; Gardner, M.; Canagarantna, M.; Yang, S.; Gonzalez-Casielles, A.; Witonsky, S.; Bhatia, P.; Gibbs, B.; Wilkie, B.; Coy, S. L.; Kachanov, A. *Proc. SPIE-Int. Soc. Opt. Eng.* **1999**, *3853*, 28.

27. Dagdigian, P. J. *Adv. Ser. Phys. Chem.* **2005**, *16*, 129.

28. Smekal, A. *Naturwiss* **1923**, *11*, 873.

29. Akhavan, J. *Spectrochim. Acta, Part A* **1991**, *47A*, 1247.

30. McNesby, K. L.; Wolfe, J. E.; Morris, J. B.; Pesce-Rodriguez, R. A. *J. Raman Spectrosc.* **1994**, *25*, 75.

31. Hendra, P. J. Laser-Raman Spectroscopy Applied to Some Chemical Problems. Presented at Mol. Spectrosc., Proc. Conf. 4th, University of Southampton: Southampton, UK, 1968.

32. Abell, G. R.; Gillespie, C. E. Remote Sensing and Analyzing of Gaseous Materials Using Raman Radiation. U.S. Patent 3,625,613, 1971.

33. Schnur, J. M. *Application of Picosecond and Light Scattering Spectroscopies to the Study of Energetic Materials*; NRL-MR-4324; U.S. Naval Research Laboratory: Washington, DC, 1980.

34. Crosley, D. R.; Schroeder, M. A. *Development of Inverse Raman Spectroscopy for Probing Rapidly Decomposing Explosives and Propellants*; ARBRL-TR-02345; U.S. Army Ballistics Research Laboratory: Aberdeen Proving Ground, MD, 1981.

35. Carver, F. W. S.; Sinclair, T. J. *J. Raman Spectrosc.* **1983**, *14*, 410.

36. Trott, W. M.; Renlund, A. M. *Appl. Opt.* **1985**, *24*, 1520.

37. Hodges, C. M.; Akhavan, J. *Spectrochim. Acta, Part A* **1990**, *46A*, 303.

38. Grisch, F.; Pealat, M.; Bouchardy, P.; Taran, J. P.; Bar, I.; Heflinger D.; Rosenwaks, S.; *Appl. Phys. Lett.* **1991**, *59*, 3516.

39. Hare, D. E.; Lee, I.-Y. S.; Hill, J. R.; Franken, J.; Suzuki, H.; Baer, B. J.; Chronister, E. L.; Dlott, D. D. *Mater. Res. Soc. Symp. Proc.* **1996**, *418*, 337.

40. Gupta, Y. M.; Pangilinan, G. I.; Winey, J. M.; Constantinou, C. P. *Chem. Phys. Lett.* **1995**, *232*, 341.

41. Cheng, C.; Kirkbride, T. E.; Batchelder, D. N.; Lacey, R. J.; Sheldon, T. G. *J. Forensic. Sci.* **1995**, *40*, 31.

42. Lewis, I. R.; Daniel, N. W., Jr.; Chaffin, N. C.; Griffiths, P. R.; Tungol, M. W. *Spectrochim. Acta, Part A* **1995**, *51A*, 1985.

43. Lacey, R. J.; Hayward, I. P.; Sands, H. S.; Batchelder, D. N. *Proc. SPIE-Int. Soc. Opt. Eng.* **1997**, *2937*, 100.

44. Sands, H. S.; Hayward, I. P.; Kirkbride, T. E.; Bennett, R.; Lacey, R. J.; Batchelder, D. N. *J. Forensic. Sci.* **1998**, *43*, 509.

45. Blanco, A.; Pacheco-Londono, L. C.; Pena-Quevedo, A. J.; Hernandez-Rivera, S. P. *Proc. SPIE-Int. Soc. Opt. Eng.* **2006**, *6217*, 621737/1.

46. Daniel, N. W., Jr.; Lewis, I. R.; Griffiths, P. R. *Mikrochim. Acta, Suppl.* **1997**, *14*, 281.

47. Lewis, I. R.; Daniel, N. W., Jr.; Griffiths, P. R. *Appl. Spectrosc.* **1997**, *51*, 1854.

48. Moore, D. S.; Fresen, J. *Anal. Chem.* **2001**, *369*, 393.

49. Hass, J. W., III; Sylvia, J. M.; Spencer, K. M.; Johnston, T. W.; Clauson, S. L. *Proc. SPIE-Int. Soc. Opt. Eng.* **1998**, *3392*, 469.

50. Spencer, K. M.; Sylvia, J. M.; Janni, J. A.; Klein, J. D. *Proc. SPIE-Int. Soc. Opt. Eng.* **1999**, *3710*, 373.

51. Sylvia, J. M.; Janni, J. A.; Klein, J. D.; Spencer, K. M. *Anal. Chem.* **2000**, *72*, 5834.

52. Bertone, J. F.; Cordeiro, K. L.; Sylvia, J. M.; Spencer, K. M. *Proc. SPIE-Int. Soc. Opt. Eng.* **2004**, *5403*, 387.

53. Baker, G. A.; Moore, D. S. *Anal. Bioanal. Chem.* **2005**, *382*, 1751.

54. Dieringer, J. A.; McFarland, A. D.; Shah, N. C.; Stuart, D. A.; Whitney, A. V.; Yonzon, C. R.; Young, M. A.; Zhang, X.; Van Duyne, R. P. *Faraday Discuss.* **2006**, *132*, 9.

55. Hirschfeld, T. *Appl. Opt.* **1974**, *13*, 1435.

56. Hirschfeld, T.; Schildkraut, E. R.; Tannenbaum, H.; Tanenbaum, D. *Appl. Phys. Lett.* **1973**, *22*, 38.

57. Angel, S. M.; Kulp, T. J.; Vess, T. M. *Appl. Spectrosc.* **1992**, *46*, 1085.

58. Lucey, P. G.; Cooney, T. F.; Sharma, S. K. *P. Lunar Planet Sci. C.* **1998**, *29*, 1354.

59. Sharma, S. K.; Misara, A. K.; Sharma, B. *Spectrochim. Acta, Part A* **2005**, *61A*, 2404.

60. Sharma, S. K.; Misara, A. K.; Lucey, P. G.; Angel, S. M.; McKay, C. P. *Appl. Spectrosc.* **2006**, *60*, 871.

61. Wu, M.; Ray, M.; Fung, K. H.; Ruckman, M. W.; Harder, D.; Sedlacek, A. J., III. *Appl. Spectrosc.* **2000**, *54*, 800.

62. Long, D. A. *Raman Spectroscopy*; McGraw-Hill: New York, 1977.

63. Asher, S. A.; Johnson, C. R. *Science* **1984**, *225*, 311.

64. Dudik, J. M.; Johnson, C. R.; Asher, S. A. *J. Chem. Phys.* **1985**, *82*, 1732.

65. Anderson, G. P.; Berk, A.; Achary, P. K.; Matthew, M. W.; Bernstein, L. S.; Chetwynd, J. H.; Dothe, H.; Adler-Golden, S. M.; Ratkowski, A. J.; Felde, G. W.; Gardner, J. A.; Hoke, M. L.; Richtsmeier, S. C.; Pukall, B.; Mello, J.; Jeong, L. S. *Proc. SPIE-Int. Soc. Opt. Eng.* **2000**, *4049*, 176.

66. Carter, J. C.; Angel, S. M.; Lawrence-Snyder, M.; Scaffidi, J.; Whipple, R. E.; Reynolds, J. G. *Appl. Spectrosc.* **2005**, *59*, 769.

67. Ray, M. D.; Sedlacek, A. J., III; Wu, M. *Rev. Sci. Instrum.* **2000**, *71*, 3485.

68. Higdon, N. S.; Chyba, T. H.; Richter, D. A.; Ponsardin, P. L.; Armstrong, W. T.; Lobb, C. T.; Kelly, B. T.; Babnick, R. D.; Sedlacek, A. J., III. *Proc. SPIE-Int. Soc. Opt. Eng.* **2002**, *4722*, 50.

69. Rusak, D. A.; Castle, B. C.; Smith, B. W.; Winefordner, J. D. *Crit. Rev. Anal. Chem.* **1997**, *27*, 257.

70. Rusak, D. A.; Castle, B. C.; Smith, B. W.; Winefordner, J. D. *TrAC* **1998**, *17*, 453.

71. Schechter, I. *Rev. Anal. Chem.* **1997**, *16*, 173.

72. Anzano, J. M.; Gornushkin, I. B.; Smith, B. W.; Winefordner, J. D. *Polym. Eng. Sci.* **2000**, *40*, 2423.

73. DeLucia, F. C., Jr.; Samuels, A. C.; Harmon, R. S.; Walters, R. A.; McNesby, K. L.; LaPointe, R.; Winkel, R. J., Jr.; Miziolek, A. W. *IEEE Sensors Journal* **2005**, *5*, 681.

74. Ferioli, F.; Buckley, S. G. *Combust. Flame* **2006**, *144*, 435.

75. Hybl, J. D.; Lithgow, G. A.; Buckley, S. G. *Appl. Spectrosc.* **2003**, *57*, 1207.

76. Portnov, A.; Rosenwaks, S.; Bar, I. *Appl. Opt.* **2003**, *42*, 2835.

77. Samuels, A. C.; DeLucia, F. C., Jr.; McNesby, K. L.; Miziolek, A. W. *Appl. Opt.* **2003**, *42*, 6205.

78. Tran, M.; Sun, S.; Smith, B. W.; Winefordner, J. D. *J. Anal. At. Spectrom.* **2001**, *16*, 628.

79. DeLucia, F. C., Jr.; Harmon, R. S.; McNesby, K. L.; Winkel, R. J., Jr.; Miziolek, A. W. *Appl. Opt.* **2003**, *42*, 6148.

80. Yamamoto, K. Y.; Cremers, D. A.; Ferris, M. J.; Foster, L. E. *Appl. Spectrosc.* **1996**, *50*, 222.

81. Grönlund, R.; Lundqvist M.; Svanberg, S. *Opt. Lett.* **2005**, *30*, 2882.

82. Lopez-Moreno, C.; Palanco, S.; Javier Laserna, J.; De Lucia, F., Jr.; Miziolek, A. W.; Rose, J.; Walters, R. A.; Whitehouse, A. I. *J. Anal. At. Spectrom.* **2006**, *21*, 55.

83. Palanco, S.; Lopez-Moreno, C.; Laserna, J. J. *Spectrochim. Acta, Part B* **2006**, *61*, 88.

84. Salle, B.; Lacour, J. L.; Vors, E.; Fichet, P.; Maurice, S.; Cremers, D. A.; Wiens, R. C. *Spectrochim. Acta, Part B* **2004**, *59*, 1413.

85. Corsi, M.; Cristoforetti, G.; Giuffrida, M.; Hidalgo, M.; Legnaioli, S.; Palleschi, V.; Salvetti, A.; Tognoni, E.; Vallebona, C. *Spectrochim. Acta, Part B* **2004**, *59*, 723.

86. Gautier, C.; Fichet, P.; Menut, D.; Lacour, J.- L.; L'Hermite, D.; Dubessy, J. *Spectrochim. Acta, Part B* **2005**, *60*, 792.

87. Scaffidi, J.; Angel, S. M.; Cremers, D. A. *Anal. Chem.* **2006**, *78*, 24.

88. Stratis, D. N.; Eland, K. L.; Angel, S. M. *Appl. Spectrosc.* **2000**, *54*, 1270.

89. Eland, K. L.; Stratis, D. N.; Gold, D. M.; Goode, S. R.; Angel, S. M. *Appl. Spectrosc.* **2001**, *55*, 286.

90. Le Drogoff, B.; Margot, J.; Chaker, M.; Sabsabi, M.; Barthelemy, O.; Johnston, T. W.; Laville, S.; Vidal, F.; von Kaenel, Y. *Spectrochimica Acta Part B* **2001**, *56*, 987.

91. Liu, X.; Du, D.; Mourou, G. *IEEE J. Quant. Electron.* **1997**, *33*, 1706.

92. Dikmelik, Y.; Spicer, J. B. *Proc. SPIE-Int. Soc. Opt. Eng.* **2005**, *5794*, 757.

93. Woodward, R. M. *Proc. SPIE-Int. Soc. Opt. Eng.* **2004**, *5617*, 341.

94. Holland, W. S.; Greaves, J. S.; Zuckerman, B.; Webb, R. A.; McCarthy, C.; Coulson, I. M.; Wulther, D. M.; Dent, W. R. F.; Gear, W. K.; Robson, I. *Nature* **1998**, *392*, 788.

95. Beard, M. C.; Turner, G. M.; Schmuttenmaer, C. A. *J. Phys. Chem. B* **2002**, *106*, 7146.

96. Ferguson, B.; Zhang, X.-C. *Nat. Mater.* **2002**, *1*, 26.

97. Mittleman, D. M. *Sensing With Terahertz Radiation Berlin*; Springer-Verlag: New York, 2003.

98. Nuss, M. C.; Orenstein, J. *Millimeter and Submillimeter Wave Spectroscopy of Solids G. Gruner*; Springer-Verlag: Berlin, 1998.

99. Siegel, P. H. *IEEE T. Microw. Theory* **2004**, *52*, 2438.

100. Auston, D. H.; Cheung, K. P.; Valdmanis, J. A.; Kleinman, D. A. *Phys. Rev. Lett.* **1984**, *53*, 1555.

101. Fattinger, C.; Grischkowsky, D. *Appl. Phys. Lett.* **1988**, *53*, 1480.

102. Schmuttenmaer, C. A. *Chem. Rev.* **2004**, *104*, 1759.

103. Hangyo, M.; Tani, M.; Nagashima, T. *Int. J. Infrared Milli.* **2005**, *26*, 1661.

104. Mittleman, D. M.; Gupta, M.; Neelamani, R.; Baraniuk, R. G.; Rudd, J. V.; Koch, M. *Appl. Phys. B* **1999**, *68*, 1085.

105. Hangyo, M.; Nagashima, T.; Nashima, S. *Meas. Sci. Technol.* **2002**, *13*, 1727.

106. Nashima, S.; Morikawa, O.; Takata, K.; Hangyo, M. *Appl. Phys. Lett.* **2001**, *79*, 3923.

107. Woodward, R. M. *Proc. SPIE-Int. Soc. Opt. Eng.* **2005**, *5781*, 22.

108. Kemp, M. C.; Taday, P. F.; Cole, B. E.; Cluff, J. A.; Fitzgerald, A. J.; Tribe, W. R. *Proc. SPIE-Int. Soc. Opt. Eng.* **2003**, *5070*, 44.

109. Chantry, G. W. Submillimetre Spectroscopy: *A Guide to the Theoretical and Experimental Physics of the Far Infrared*; Academic Press Inc., Ltd.: London, 1971.

110. Hu, B. B.; Nuss, M. C. *Opt. Lett.* **1995**, *20*, 1716.

111. Ferguson, B.; Wang, S.; Zhong, H.; Abbott, D.; Zhang, X.-C. *Proc. SPIE-Int. Soc. Opt. Eng.* **2003**, *5070*, 7.

112. Mittleman, D. M.; Hunsche, S.; Boivin, L.; Nuss, M. C. *Opt. Lett.* **1997**, *22*, 904.

113. Xu, J. Z.; Liu, H. B.; Yuan, T.; Kersting, R.; Zhang, X.-C. *Proc. SPIE-Int. Soc. Opt. Eng.* **2003**, *5070*, 17.

114. van Exter, M.; Fattinger C.; Grischkowsky, D. *Opt. Lett.* **1989**, *14*, 1128.

115. Yuan, T.; Liu, H. B.; Xu, J. Z.; Al-Douseri, F.; Hu, Y.; Zhang, X.-C. *Proc. SPIE-Int. Soc. Opt. Eng.* **2003**, *5070*, 28.

116. Baker, C.; Tribe, W. R.; Lo, T.; Cole, B. E.; Chandler, S.; Kemp, M. C. *Proc. SPIE-Int. Soc. Opt. Eng.* **2005**, *5790*, 1.

117. Woodward, R. M.; Appleby, R. *Proc. SPIE-Int. Soc. Opt. Eng.* **2005**, *5780*, 145.

118. Choi, M. K.; Bettermann, A.; Weide, D. W. v. d. *Philos. T. Roy. Soc. A* **2004**, *362*, 337.

119. Federici, J. F.; Schulkin, B.; Huang, F.; Gary, D.; Barat, R.; Oliveira, F.; Zimdars, D. *Semicond. Sci. Tech.* **2005**, *20*, S266.

120. Tribe, W. R.; Newnham, D. A.; Taday, P. F.; Kemp, M. C. *Proc. SPIE-Int. Soc. Opt. Eng.* **2004**, *5354*, 168.

121. Woolard, D. L.; Brown, E. R.; Pepper, M.; Kemp, M. C. *P. IEEE* **2005**, *93*, 1722.

122. Lo, T.; Gregory, I. S.; Baker, C.; Taday, P. F.; Tribe, W. R.; Kemp, M. C. *Vib. Spectrosc.* **2006**, *42*, 243.

123. Chen, Y.; Liu, H. B.; Deng, Y.; Schauki, D.; Fitch, M. J.; Osiander, R.; Dodson, C.; Spicer, J. B.; Shur, M.; Zhang, X.-C. *Chem. Phys. Lett.* **2004**, *400*, 357.

124. Osiander, R.; Miragliotta, J. A.; Jiang, Z.; Xu, J. Z.; Zhang, X.-C. *Proc. SPIE-Int. Soc. Opt. Eng.* **2003**, *5070*, 1.

125. Yamamoto, K.; Yamaguchi, M.; Miyamaru, F.; Tani, M.; Hangyo, M.; Ikeda, T.; Matsushita, A.; Koide, K.; Tatsuno, M.; Minami, Y. *Jpn. J. Appl. Phys.* **2004**, *43*, L414.

126. Cook, D. J.; Decker, B. K.; Maislin, G.; Allen, M. G. *Proc. SPIE-Int. Soc. Opt. Eng.* **2004**, *5354*, 55.

127. Funk, D. J.; Calgaro, F.; Averitt, R. D.; Asaki, M. L. T.; Taylor, A. J. *Appl. Spectrosc.* **2004**, *58*, 428.

128. Cook, D. J.; Decker, B. K.; Allen, M. G. Quantitative Thz Spectroscopy of Explosive Materials. Presented at Optical Terahertz Science and Technology, Orlando, FL, 2005,

129. Liu, H. -B.; Chen, Y.; Bastiaans, G. J.; Zhang, X.-C. *Opt. Express* **2006**, *14*, 415.

130. Huang, F.; Schulkin, B.; Altan, H.; Federici, J. F.; Gary, D.; Barat, R.; Zimdars, D.; Chen, M.; Tanner, D. B. *Appl. Phys. Lett.* **2004**, *85*, 5535.

131. Shen, Y. C.; Lo, T.; Taday, P. F.; Cole, B. E.; Tribe, W. R.; Kemp, M. C. *Appl. Phys. Lett.* **2005**, *86*, 241116.

132. Brand, H. V.; Rabie, R. L.; Funk, D. J.; Diaz-Acosta, I.; Pulay, P.; Lippert, T. K. *J. Phys. Chem. B* **2002**, *106*, 10594.

133. Gruzdkov, Y. A.; Gupta, Y. M. *J. Phys. Chem. A* **2001**, *105*, 6197.

134. Barber, J.; Hooks, D. E.; Funk, D. J.; Averitt, R. D.; Taylor, A. J.; Babikov, D. *J. Phys. Chem. A* **2005**, *109*, 3501.

135. Allis, D. G.; Prokhorova, D. A.; Korter, T. M. *J. Phys. Chem. A* **2006**, *110*, 1951.

136. Kawase, K.; Ogawa, Y.; Wantanabe, Y. *Proc. SPIE-Int. Soc. Opt. Eng.* **2004**, *5354*, 63.

137. Oliveira, F.; Barat, R.; Schulkin, B.; Huang, F.; Federici, J. F.; Gary, D.; Zimdars, D. *Proc. SPIE-Int. Soc. Opt. Eng.* **2004**, *5411*, 45.

138. Zhong, H. Terahertz Wave Reflective Sensing and Imaging. Doctoral dissertation, Rensselaer Polytechnic Instituite, 2006.

139. Claspy, P. C.; Pao, Y.-H.; Kwong, S.; Nodov, E. *Appl. Opt.* **1976**, *15*, 1506.

140. Crane, R. A. *Appl. Opt.* **1978**, *17*, 2097.

141. Clark, A.; Ledingham, K. W. D.; Marshall, A.; Sander, J.; Singhal, R. P. *Analyst* **1993**, *118*, 601.

142. Lemire, G. W.; Simeonsson, J. B.; Sausa, R. C. *Anal. Chem.* **1993**, *65*, 529.

143. Simeonsson, J. B.; Lemire, G. W.; Sausa, R. C. *Appl. Spectrosc.* **1993**, *47*, 1907.

144. Daugey, N.; Shu, J.; Bar, I.; Rosenwaks, S. *Appl. Spectrosc.* **1999**, *53*, 57.

145. Mullen, C.; Irwin, A.; Pond, B. V.; Huestis, D. L.; Coggiola, M. J.; Oser, H. *Anal. Chem.* **2006**, *78*, 3807.

146. Shu, J.; Bar, I.; Rosenwaks, S. *Appl. Opt.* **1999**, *38*, 4705.

147. Zuckermann, H.; Greenblatt, G. D.; Haas, Y. *J. Phys. Chem.* **1987**, *91*, 5159.

148. Swayambunathan, V.; Singh, G.; Sausa, R. C. *Appl. Opt.* **1999**, *38*, 6447.

149. Cabalo, J.; Sausa, R. *Appl. Spectrosc.* **2003**, *57*, 1196.

150. Claspy, P. C.; Pao, Y.-H.; Kwong, S.; Nodov, E. *IEEE J. Quant. Electron.* **1975**, *11*, D37.

151. Prasad, R. L.; Prasad, R.; Bhar, G. C.; Thakur, S. N. *Spectrochim. Acta, Part A* **2002**, *58*, 3093.

152. Zhu, J.; Lustig, D.; Sofer, I.; Lubman, D. M. *Anal. Chem.* **1990**, *62*, 2225.

153. Ramos, C.; Dagdigian, P. J. *Appl. Opt.* **2007**, *46*, 620.

154. Shu, J.; Bar, I.; Rosenwaks, S. *Appl. Phys. B* **2000**, *70*, 621.

155. Usachev, A. D.; Miller, T. S.; Singh, J. P.; Yueh, F. Y.; Jang, P. R.; Monts, D. L. *Appl. Spectrosc.* **2001**, *55*, 125.

156. Wu, D. D.; Singh, J. P.; Yueh, F. Y.; Monts, D. L. *Appl. Opt.* **1996**, *35*, 3998.

157. Boudreaux, G. M.; Miller, T. S.; Kunefke, A. J.; Singh, J. P.; Yueh, F.-Y.; Monts, D. L. *Appl. Opt.* **1999**, *38*, 1411.

158. Arusi-Parpar, T.; Heflinger, D.; Lavi, R. *Appl. Opt.* **2001**, *40*, 6677.

159. Heflinger, D.; Arusi-Parpar, T.; Ron, Y.; Lavi, R. *Opt. Comm.* **2002**, *204*, 327.

160. Simonson, R. J.; Hance, B. G.; Schmitt, R. L.; Johnson, M. S.; Hargis, P. J., Jr. *Proc. SPIE-Int. Soc. Opt. Eng.* **2001**, *4394*, 879.

161. Mullen, C.; Huestis, D.; Coggiola, M.; Oser, H. *Int. J. Mass Spectrom.* **2006**, *252*, 69.

162. Smit, K. J. *J. Energ. Mat.* **1991**, *9*, 81.

163. Huang, S. D.; Kolaitis, L.; Lubman, D. M. *Appl. Spectrosc.* **1987**, *41*, 1371.

164. Morgan, J. S.; Bryden, W. A.; Miragliotta, J. A.; Aamodt, L. C. *Johns Hopkins APL Technical Digest* **1999**, *20*, 389.

165. Ledingham, K. W. D. *Physica Scripta* **1995**, *T58*, 100.

166. Simeonsson, J. B.; Sausa, R. C. *Appl. Spectrosc. Rev.* **1996**, *31*, 1.

167. Simeonsson, J. B.; Sausa, R. C. *Appl. Spectrosc.* **1996**, *50*, 1277.

168. Simeonsson, J. B.; Sausa, R. C. *TrAC* **1998**, *17*, 550.

169. Marshall, A.; Clark, A.; Ledingham, K. W. D.; Sander, J.; Singhal, R. P. *Int. J. Mass Spectrom. Ion Processes* **1993**, *125*, R21.

170. Marshall, A.; Clark, A.; Jennings, R.; Ledingham, K. W. D.; Sander, J.; Singhal, R. P. *Int. J. Mass Spectrom. Ion Processes* **1992**, *116*, 143.

171. Marshall, A.; Clark, A.; Jennings, R.; Ledingham, K. W. D.; Singhal, R. P. *Int. J. Mass Spectrom. Ion Processes* **1992**, *112*, 273.

172. Kosmidis, C.; Marshall, A.; Clark, A.; Deas, R. M.; Ledingham, K. W. D.; Singhal, R. P. *Rapid Commun. Mass Spectrom.* **1994**, *8*, 607.

173. Pastel, R. L.; Sausa, R. C. *Appl. Opt.* **1996**, *35*, 4046.

174. Schmidt, S.; Appel, M. F.; Garnica, R. M.; Schindler, R. N.; Benter, T. *Anal. Chem.* **1999**, *71*, 3721.

175. Simeonsson, J. B.; Lemire, G. W.; Sausa, R. C. *Anal. Chem.* **1994**, *66*, 2272.

176. Guizard, S.; Chapoulard, D.; Horani, M.; Gauyacq, D. *Appl. Phys. B* **1989**, *48*, 471.

177. Pastel, R. L.; Sausa, R. C. *Appl. Opt.* **2000**, *39*, 2487.

178. Sausa, R. C.; Swayambunathan, V.; Singh, G. *Detection of Energetic Materials by Laser Photofragmentation/Fragment Detection and Pyrolysis/Laser-Induced Fluorescence*; ARL-TR-2387; U.S. Army Research Laboratory: Aberdeen Proving Ground, MD, 2001.

179. Rodgers, M. O.; Asai, K.; Davis, D. D. *Appl. Opt.* **1980**, *19*, 3597.

180. Guo, Y. Q.; Greenfield, M.; Bernstein, E. R. *J. Chem. Phys.* **2005**, *122*, 244310.

181. Shu, J.; Bar, I.; Rosenwaks, S. *Appl. Phys. B* **2000**, *71*, 665.

182. Ledingham, K. W. D.; Singhal, R. P. *Int. J. Mass Spectrom. Ion Processes* **1997**, *163*, 149.

183. Kosmidis, C.; Ledingham, K. W. D.; Kilic, H. S.; McCanny, T.; Singhal, R. P.; Langley, A. J.; Shaikh, W. *J. Phys. Chem. A* **1997**, *101*, 2264.

184. Tonnies, K.; Schmid, R. P.; Weickhardt, C.; Reif, J.; Grotemeyer, J. *Int. J. Mass Spectrom.* **2001**, *206*, 245.

185. Weickhardt, C.; Tonnies, K. *Rapid Commun. Mass Spectrom.* **2002**, *16*, 442.

186. Hankin, S. M.; Tasker, A. D.; Robson, L.; Ledingham, K. W. D.; Fang, X.; McKenna, P.; McCanny, T.; Singhal, R. P.; Kosmidis, C.; Tzallas, P.; Jaroszynski, D. A.; Jones, D. R.; Issac, R. C.; Jamison, S. *Rapid Commun. Mass Spectrom.* **2002**, *16*, 111.

187. Osorio, C.; Gomez, L. M.; Hernandez, S. P.; Castro, M. E. *Proc. SPIE-Int. Soc. Opt. Eng.* **2005**, *5794*, 803.

188. Hasue, K.; Nakahara, S.; Morimoto, J.; Yamagami, T.; Okamoto, Y.; Miyakawa, T. *Propell. Explos. Pyrot.* **1995**, *20*, 187.

189. Rosengren, L.-G. *Appl. Opt.* **1975**, *14*, 1960.

190. Angus, A. M.; Marinero, E. E.; Colles, M. J. *Opt. Comm.* **1975**, *14*, 223.

191. Webber, M. E.; Pushkarsky, M.; Patel, C. K. N. *Appl. Opt.* **2003**, *42*, 2119.

192. Kreuzer, L. B.; Kenyon, N. D.; Patel, C. K. N. *Science* **1972**, *177*, 347.

193. Claspy, P. C.; Ha, C.; Pao, Y.-H. *Appl. Opt.* **1977**, *16*, 2972.

194. Terhune, R. W.; Anderson, J. E. *Opt. Lett.* **1977**, *1*, 70.

195. Fried, A. *Appl. Spectrosc.* **1982**, *36*, 562.

196. Xiang, N.; Sabatier, J. M. *J. Acoust. Soc. Am.* **2003**, *113*, 1333.

197. Bromenshenk, J. J.; Henderson, C. B.; Smith, G. C. *Appendix S: Biological Systems (Paper Ii) in Alternatives for Landmine Detection*; MacDonald, J., Lockwood, J. R., McFee, J., Altshuler, T., Broach, T., Carin, L., Harmon, R., Rappaport, C., Scott, W., Weaver, R., Eds.; RAND Corp.: Santa Monica, CA, 2003; p 273.

198. Repasky, K. S.; Shaw, J. A.; Scheppele, R.; Melton, C.; Carsten, J. L.; Spangler, L. H. *Appl. Opt.* **2006**, *45*, 1839.

199. Shaw, J. A.; Seldomridge, N. L.; Dunkle, D. L.; Nugent, P. W.; Spangler, L. H.; Bromenshenk, J. J.; Henderson, C. B.; Churnside, J. H.; Wilson, J. J. *Opt. Express* **2005**, *13*, 5853.

200. Germanenko, I. N.; Li, S. T.; El-Shall, M. S. *J. Phys. Chem. B* **2001**, *105*, 59.

List of Symbols, Abbreviations, and Acronyms

ARL	U.S. Army Research Laboratory
C-4	RDX (91%)
CARS	Coherent Anti-Stokes Raman spectroscopy
CRDS	Cavity ringdown spectroscopy
CW	Continuous wave
DEGDN	Diethylene glycol dinitrate
DIAL	Differential absorption LIDAR
DNB	Dinitrobenzene
DNT	Dinitrotoluene
EGDN	Ethyleneglycol dinitrate
EM	Energetic material
ERC	Energetic related compound
FT	Fourier transform
FT-Raman	Fourier transform Raman spectroscopy
GC	Gas chromatography
HMX	Octahydro-1,3,5,7-tetrocine
IR	Infrared
IRDIAL	Infrared differential absorption LIDAR
IRMPD	Infrared multiphoton dissociation
JA2	NC (60%), NG (15%), DEGDN (25%)
LD	Laser desorption
LDV	Laser Doppler vibrometer
LIBS	Laser-induced breakdown spectroscopy
LIDAR	Light detection and ranging

LIF	Laser-induced fluorescence
LOD	Limits of detetection
LSPR	Localized surface plasmon resonance
M30	NQ (50%), NC (30%), NG (15%)
M9	NC (60%), NG (40%)
Metabel	PETN-based sheet explosive
MS	Mass spectrometry
NB	Nitrobenzene
NC	Nitrocellulose
Nd:YAG	Neodinium Ytterium aluminum garnet
NG	Nitroglycerine
NQ	Nitroguanidine
NT	Nitrotoluene
OPO	Optical parametric oscillator
PAS	Photoacoustic spectroscopy
PE4	Similar to C-4 (RDX-based) with different binders
PETN	Pentaerythritol tetranitrate
PF-FD	Photofragmentation fragment detection spectroscopy
PF-LIF	Photofragmentation laser-induced fluorescence spectroscopy
PF-REMPI	Photofragmentation-resonance enhanced multiphoton ionization
pg	Picograms
ppb	Parts per billion
ppm	Parts per million
ppq	Parts per quadrillion
ppt	Parts per trillion
QC	Quantum cascade
RDX	Hexahydro-1,3,5-trinitro-s-trazine

REMPI	Resonance-enhanced multiphoton ionization
R2PI	Resonant two-photon ionization
Semtex H	PETN (49.8%), RDX (50.2%)
SERS	Surface enhanced Raman spectroscopy
SFG	Sum-frequency generation spectroscopy
SMSERS	Single molecule SERS
SPF-FD	Surface photofragmentation-fragment detection
SPF-REMPI	Surface photofragmentaion-resonance enhanced multiphoton ionization
SPI	Single photon laser ionization
STP	Standard temperature and pressure
SX2	RDX-based sheet explosive
TATB	Triaminotrinitro benzene
TATP	Triacetone triperoxide
TDLAS	Tunable diode laser spectroscopy
Tetryl	2,4,6-trinitrophenyl-N-methylnitramine
THz	Terahertz
THz-TDS	Terahertz time domain spectroscopy
TNT	Trinitrotoluene
TOF	Time of flight
TOFMS	Time of flight mass spectrometry
TRDX	Hexahydro-1,3,5-trinitoso-s-trazine
UV	Ultraviolet
UV/Vis	Ultraviolet visible spectroscopy
VUV	Vacuum ultraviolet

NO. OF
COPIES   ORGANIZATION

   1   DEFENSE TECHNICAL
 (PDF   INFORMATION CTR
 ONLY)   DTIC OCA
         8725 JOHN J KINGMAN RD
         STE 0944
         FORT BELVOIR VA 22060-6218

   1   US ARMY RSRCH DEV &
         ENGRG CMD
         SYSTEMS OF SYSTEMS
         INTEGRATION
         AMSRD SS T
         6000 6TH ST STE 100
         FORT BELVOIR VA 22060-5608

   1   DIRECTOR
         US ARMY RESEARCH LAB
         IMNE ALC IMS
         2800 POWDER MILL RD
         ADELPHI MD 20783-1197

   3   DIRECTOR
         US ARMY RESEARCH LAB
         AMSRD ARL CI OK TL
         2800 POWDER MILL RD
         ADELPHI MD 20783-1197

         ABERDEEN PROVING GROUND

   1   DIR USARL
         AMSRD ARL CI OK TP (BLDG 4600)

NO. OF COPIES	ORGANIZATION	NO. OF COPIES	ORGANIZATION
1	CHEMICAL SCI DIV OAK RIDGE NATL LAB G BAKER PO BOX 2008 OAK RIDGE TN 37831-6110	1	TRANSPORTATION SEC LAB OFFICE OF RESEARCH AND DEV R LAREAU BLDG 315 TSL 200 ATLANTIC CITY INTL AIRPORT NJ 08405
1	G FOGG 2231 CRYSTAL DR STE 900 ARLINGTON VA 22202	1	NATL CTR FOR FORENSIC SCI UNIV OF CENTRAL FLORIDA M SIGMAN PO BOX 162367 ORLANDO FL 32816-2367
1	CHEMIMAGE P TREADO 7301 PENN AVE PITTSBURGH PA 15208	1	NATL DYNAMICS GROUP DYNAMIC EXPERIMENTATION DIV D MOORE MS P952 LOS ALAMOS NM 87545
1	A3 TECHLGY LLC R RUSSO PO BOX 5049 WALNUT CREEK CA 94596	1	D DIETZ ATSE DOT CM 320 MANSCEN LOOP STE 115 FORT LEONARD WOOD MO 65473-8929
1	BATTELLE EASTERN SCI & TECHLGY CTR C MULLINS 1204 TECHLGY DR ABERDEEN MD 21001-1228	1	RAPID EQUIPPING FORCE J GEDDES 10236 BURBECK RD FORT BELVOIR VA 22060-5852
1	BAE SYSTEMS TECHLGY SOLUTIONS SECTOR SYSTEMS ENGRG SOLUTIONS J ERDMANN PO BOX 381 DAHLGREN VA 22448-0381	1	US DEPT OF HOMELAND SEC SCIENCE AND TECHLGY M SHEPARD 245 MURRAY LANE SW WASHINGTON DC 20528
1	WHITING SCHOOL OF ENGRG 120 NEW ENGRG BLDG M DONAHUE 3400 N CHARLES ST BALTIMORE MD 21218-2681	1	G GILBERT MCMR ZB T 504 SCOTT ST FORT DETRICK MD 21702-5012
1	BATTELLE EASTERN SCI & TECHLGY CTR B JEZEK 1204 TECHNLGY DR ABERDEEN MD 21001-1228	1	MENTIS SCIENCES J PLUMER 150 DOW ST TOWER 2 MANCHESTER NH 03101
1	IDAHO NATL LAB E CESPEDES PO BOX 1625 IDAHO FALLS ID 83415-3690	1	NIGHT VISION AND ELECT SENSORS DIR A LAPOINTE 10221 BURBECK RD FORT BELVOIR VA 22060

1	NIGHT VISION AND ELECT SENSORS DIR K SHIRBANDI 10221 BURBECK RD FORT BELVOIR VA 22060
1	R WINKEL DEPT OF PHYSICS USMA WEST POINT NY 10996-1790
1	US ARMY RESEARCH OFC R HARMON 4300 S MIAMI BLVD DURHAM NC 27709-2211

J GOTTFRIED
M GRAMS
K MCNESBY
R BEYER
B RICE
B HOMAN
J NEWBERRY
C MUNSON

ABERDEEN PROVING GROUND

1 US ARMY ATC
   CSTE DTC AT SL F
   C SIMPSON
   400 COLLERAN RD
   APG MD 21005-5059

1 US ARMY ATC
   CSTE DTC AT SL F
   W BOLT
   400 COLLERAN RD
   APG MD 21005-5059

1 CAMBER CORP
   G SCHEFFLER
   5183 BLACKHAWK RD
   BLDG E3549
   APG MD 21010-5424

1 A FOUNTAIN III
   AMSRD ECB RT D
   BLDG E3330/147
   APG-EA MD 21010-5424

18 DIR USARL
    AMSRD ARL WM B
      M ZOLTOSKI
      C FORD
      J MORRIS
    AMSRD ARL WM BD
      S PIRAINO
      R PESCE-RODRIGEZ
      R SAUSA
      F DELUCIA JR
      A MIZIOLEK
      P KASTE
      B FORCH

INTENTIONALLY LEFT BLANK.